

*Digital Comprehensive Summaries of Uppsala Dissertations
from the Faculty of Science and Technology 2365*

Elucidating Chemical and Electrochemical Side-Reaction Mechanisms in Li-ion Batteries

NEEHA GOGOI



ACTA UNIVERSITATIS
UPSALIENSIS
2024

ISSN 1651-6214
ISBN 978-91-513-2037-3
urn:nbn:se:uu:diva-523121



UPPSALA
UNIVERSITET

Dissertation presented at Uppsala University to be publicly examined in Polhemsalen, Ångströmlaboratoriet, Lägerhyddsvägen 1, Uppsala, Friday, 5 April 2024 at 09:15 for the degree of Doctor of Philosophy. The examination will be conducted in English. Faculty examiner: Professor M. Rosa Palacín (Institut de Ciencia de Materials de Barcelona).

Abstract

Gogoi, N. 2024. Elucidating Chemical and Electrochemical Side-Reaction Mechanisms in Li-ion Batteries. *Digital Comprehensive Summaries of Uppsala Dissertations from the Faculty of Science and Technology* 2365. 77 pp. Uppsala: Acta Universitatis Upsaliensis. ISBN 978-91-513-2037-3.

Lithium-ion batteries constitute a leading technology that plays a major role in the transition towards sustainable transportation and power generation. The stability of modern batteries relies on a passivation layer formed on the negative electrode known as the solid electrolyte interphase (SEI). Despite concerted efforts to comprehend the various processes taking place during SEI formation, monitoring the reaction pathways in real-time is still very challenging. This is due to the complex interactions within the multicomponent electrochemical system, aggravated by the wide range of electrolyte compositions, electrode materials, and operating conditions.

In this thesis, *operando* surface enhanced Raman spectroscopy is explored to elucidate the progressive formation of the SEI on the negative electrode surface when the electrode is negatively polarised in a spectro-electrochemical cell. Complementary online-electrochemical mass spectrometry is employed to identify the associated gaseous products formed during the process. The work illustrates that the electrolyte as well as contaminants, such as O₂, CO₂, and H₂O, contribute in electro-/chemical processes that build up the SEI. The thesis then explores reaction pathways involving a SEI-forming electrolyte additive, namely vinylene carbonate (VC), emphasizing its role as a H₂O scavenging agent. In comparison to the conventional electrolyte solvent ethylene carbonate, VC exhibits a faster reaction with water impurities, particularly in presence of hydroxide ions. This results in the formation of products that are less likely to impact cell performance.

In the later part, the thesis delves into understanding the stability of electrolyte in an environment of Lewis bases (LB) typically found in the SEI. For that, individual LB (*e.g.*, OH⁻ and OCH₃⁻) are mixed with typical carbonate-based solvents and the products formed as a result of the reaction are analysed. Furthermore, tris(trimethylsilyl)phosphate (TMSPa), a representative of the silyl-functionalised electrolyte additive and known for its reactivity, especially towards fluorides, is used as a means to chemically probe its reactivity towards several LB residues. This investigation aims to establish a more simplified and generally applicable reaction mechanism thereof. The products that are soluble in the electrolyte have been investigated by nuclear magnetic resonance spectroscopy and those in the gas phase is characterised by mass spectrometry. The work highlights that the residues that remain active even after the SEI formation may lead to unwanted side-reactions.

The thesis contributes to a deeper fundamental understanding of the myriad of processes that take place in batteries during SEI formation providing insights crucial for designing next-generation battery materials.

Keywords: Lithium-ion battery, solid electrolyte interphase, electrolyte additives, reaction mechanism, ethylene carbonate, vinylene carbonate, tris(trimethylsilyl)phosphate, surface enhanced Raman spectroscopy

Neeha Gogoi, Department of Chemistry - Ångström, Structural Chemistry, Box 538, Uppsala University, SE-751 21 Uppsala, Sweden.

© Neeha Gogoi 2024

ISSN 1651-6214

ISBN 978-91-513-2037-3

URN urn:nbn:se:uu:diva-523121 (<http://urn.kb.se/resolve?urn=urn:nbn:se:uu:diva-523121>)

“Completing this PhD was like assembling IKEA furniture—confusing at first, requires countless tools, and you're left wondering if you missed a crucial step along the way.”

- Anonymous

List of Papers

This thesis is based on the following papers, which are referred to in the text by their Roman numerals.

- I. **Gogoi, N.**, Melin T., Berg E.J., (2022) Elucidating the Step-wise Solid Electrolyte Interphase Formation in Lithium-ion Batteries with *Operando* Raman Spectroscopy. *Advanced Materials Interfaces*, 2200945¹
- II. **Gogoi, N.**, Lundström R., Hernández G., Berg E. J., (2024) Base-Driven Ring-Opening Reactions of Vinylene Carbonate, *manuscript submitted*
- III. Lundström R., **Gogoi N.**, Melin T., Berg E. J., (2024) Unveiling Reaction Pathways of Ethylene Carbonate and Vinylene Carbonate in Li-ion Batteries, *manuscript submitted*
- IV. **Gogoi, N.**, Bowall E., Lundström, R., Mozhzhukhina, N., Hernández, G., Broqvist, P., Berg, E.J., (2022) Silyl-Functionalized Electrolyte Additives and Their Reactivity toward Lewis Bases in Li-ion Cells. *Chemistry of Materials*, 34, 3831–3838²
- V. **Gogoi, N.**, Wahyudi W., Mindemark J., Hernández G., Broqvist P., Berg E.J., (2024) Reactivity of Organosilicon Additives with Water in Li-ion Batteries. *The Journal of Physical Chemistry C*, 128, 1654–1662³

Reprints were made with permission from the respective publishers.

My contribution to the papers in this thesis:

- I. Took part in the planning of the project and performed all experiments along with T. Melin. Wrote the manuscript together with the co-authors.
- II. Planned the project together with my supervisor. Performed most of the experiments and wrote manuscript with input from co-authors.

- III. Took part in the discussions, planned and performed the NMR characterisation with collaboration with the co-authors and contributed in the writing of the manuscript.
- IV. Planned experiments with the co-authors. Performed all experiments except for the computational calculations, which were performed by P. Broqvist and E. Bowall. Wrote the manuscript with inputs from the co-authors.
- V. Planned the project together with my supervisor. Performed all experiments except for the computational calculations. Wrote the manuscript with inputs from the co-authors.

Disclaimer: Parts of this thesis are based on the author's licentiate thesis titled "Elucidating the Formation of Electrode/Electrolyte Interphases in Li-ion Batteries", (Uppsala University, 2022). Reprints were made with permission from the respective publishers.

Papers not included in the thesis

- Lundström R., **Gogoi N.**, Hou X., Berg E. J. (2023) Competing Ethylene Carbonate Reactions on Carbon Electrode in Li-ion Batteries, *Journal of The Electrochemical Society*, 170, 040516⁴
- Hou X., Zhang L., **Gogoi N.**, Edström K., and Berg E. J. (2023), Interfacial Chemistry in Aqueous Lithium-Ion Batteries: A Case Study of V₂O₅ in Dilute Aqueous Electrolytes, *Small*, 2308577⁵

Contents

1	Introduction	11
1.1	Motivation for energy storage.....	11
1.2	Elementary Concepts of Lithium-ion battery.....	12
1.3	The LIB electrolyte	13
1.3.1	Lithium salts	13
1.3.2	Solvents.....	14
1.3.3	Additives.....	16
1.3.3.1	Vinylene carbonate	17
1.3.3.2	Tris(trimethylsilyl)phosphate	18
1.4	Interfacial chemistry in LIBs	19
1.4.1	Interface and interphase	19
1.4.2	Electric double layer	20
1.4.3	The solid electrolyte interphase-formation & ageing	21
1.5	Characterisation techniques for interphases.....	24
1.6	Raman spectroscopy	24
1.6.1	Principles of Raman spectroscopy	24
1.6.2	Surface-enhanced Raman spectroscopy.....	25
1.6.3	State-of-the-art SERS studies on interphases	26
1.7	Nuclear Magnetic Resonance.....	27
1.8	Online Electrochemical Mass spectrometry.....	28
2	Thesis scope.....	29
3	Experimental.....	31
3.1	SERS	31
3.2	NMR	33
3.3	Mass spectrometry	33
1.1.1.	OEMS cell assembly.....	33
3.3.1	Injection cell set-up.....	34
3.4	Other characterisation techniques	34
3.4.1	Gas chromatography mass spectrometry	34
3.4.2	Coulometric Karl-Fischer titration.....	35
4	Summary of key results and discussion.....	36
4.1	Advanced <i>operando</i> investigation of interphase formation	36
4.1.1	Determination of the SERS enhancement factor	36
4.1.2	Electrochemistry	38

4.1.3	Investigating the gas evolution	38
4.1.4	<i>Operando</i> Raman spectroscopy	40
4.1.5	Practical considerations and limitation	42
4.2	Reaction mechanisms of electrolyte additives	43
4.2.1	VC	43
4.2.1.1	Electrochemical vs. chemical reactions of VC	43
4.2.1.2	Kinetics of VC hydrolysis	49
1.2.1.1.	Identification of VC decomposition products	50
4.2.2	TMSPa	56
4.2.2.1	Mechanisms involving TMSPa and Lewis bases	56
4.2.2.2	Reactivity of TMSPa and H ₂ O	59
5	Conclusion and future outlook.....	64
6	Sammanfattning på Svenska.....	67
7	Acknowledgements.....	70
8	References	71

Abbreviations

BMSPa	Bis(trimethylsilyl)-phosphate
BOB	Bis(oxalate)borate
CV	Cyclic voltammetry
DEC	Diethyl carbonate
DFT	Density functional theory
DME	Dimethoxy ethane
DMSO	Dimethyl sulfoxide
EA	Ethyl acetate
EC	Ethylene carbonate
EDL	Electric double layer
EF	Enhancement factor
EG	Ethylene glycol
EMC	Ethyl methyl carbonate
ESW	Electrochemical stability window
FEP	Fluorinated ethylene propylene
GCMS	Gas chromatography mass spectrometry
HSQC	Heteronuclear Single Quantum Correlation
HMBC	Heteronuclear Multiple Bond Correlation
LB	Lewis base
LIB	Lithium-ion battery
LMC	Lithium methyl carbonate
LSPR	Local surface plasmon resonance
LSV	Linear sweep voltammetry
MMSPa	Mono(trimethylsilyl)-phosphate
MD	Molecular dynamics
NMR	Nuclear magnetic resonance
OCP	Open circuit potential
OEMS	Online-electrochemical mass spectrometry
ORR	Oxygen reduction reaction
Poly(VC)	Poly(vinylene carbonate)
PEG	Polyethylene glycol
Rh6G	Rhodamine 6G
SEI	Solid electrolyte interphase
SERS	Surface enhanced Raman spectroscopy
SHE	Standard hydrogen electrode

SHINERS	Shell-isolated nanoparticle-enhanced Raman spectroscopy
TFSI	Bis(trifluoromethanesulfonyl)imide
THF	Tetrahydrofuran
TMS	Tris(Trimethylsilyl)
TMS-EG	Trimethylsilyl ethylene glycol
TMSOH	Trimethylsilanol
TMSOTMS	Hexamethyldisiloxane
TMSPa	Tris(trimethylsilyl)-phosphate
VC	Vinylene carbonate

1 Introduction

1.1 Motivation for energy storage

In an age marked by constant technological advancements, flourishing populations, and an ever-increasing demand for energy, the necessity to develop efficient and sustainable energy storage solutions has become paramount. The global landscape is witnessing a profound shift towards renewable energy sources, such as solar and wind, as nations strive to mitigate environmental impacts and reduce dependence on finite fossil fuels. However, the intermittent nature of renewable energy generation poses a significant challenge to its seamless integration into existing power grids. Hence, we need a technology that supplies the energy on demand, *i.e.*, it is able to store the energy generated from these power stations, enabling us to use it later no matter what part of the year or season or day it is.⁶ There are different solutions to that, to which batteries, fuel cells and capacitors belong. One such example is the lithium-ion battery (LIB) that has ensured continuous flow of electricity in stationary or mobile mode applications even in the remotest areas, thus enabling the transition towards sustainable power generation and transport.

The interest in Li metal for usage in rechargeable devices stems from Li's large negative potential (-3.04 V vs. Standard hydrogen electrode, SHE) and high (theoretical) gravimetric capacity (3860 mAhg^{-1}).⁷ Still, Li metal has not been successfully used on a large scale as electrode material due to its high reactivity towards electrolytes and challenges associated with surface dendrite formation during operation, which in turn causes short-circuiting and thermal runaway and thus posing serious safety issues. Therefore, "intercalation" or "insertion"-type electrodes have been developed, which have the ability to host Li^+ while allowing repeated Li^+ de-/insertion over several thousands of cycles, hence the name "Li-ion" battery.⁸ One such positive electrode active material, lithium cobalt oxide (Li_xCoO_2), has an output average electrode potential is 3.7 V when paired with a Li metal negative electrode in a "half-cell" configuration.⁹ On the negative electrode side, commonly used graphite allows for greatly enhanced full-cell energy densities due to its low de-/lithiation potential (which maximizes cell voltage) and high gravimetric capacity of 372 mAhg^{-1} (compared to any other "insertion-type" negative electrode contender). Much like the phase transitions occurring in the positive electrode, the lithiation process of graphite unfolds through a series of sequential and

well-ordered stages, culminating in the formation of LiC_6 . Each stage corresponds to plateaus in the electrochemical potential observed during both charge and discharge.

In 1991, Sony first commercialised LIB combining Asahi Kasei's petroleum coke negative electrode and Goodenough's Li_xCoO_2 , and since then more such batteries based on the most reliable carbonaceous negative electrode and transition metal-based positive electrode are available in the market.¹⁰

1.2 Elementary Concepts of Lithium-ion battery

When an external load is connected to the charged Li-ion cell, the cell undergoes discharge. Li^+ move from the negative electrode to the positive electrode through the electrolyte medium and electrons conduct from the negative electrode to the positive electrode via the external circuit generating an electric current (as illustrated in Figure 1.1). The transport of Li^+ during discharge is spontaneous and the driving force is the difference in the electrochemical potential of the Li in the two electrodes. During charge, the same process takes place, but in opposite direction. Figure 1.1 depicts a typical Li-ion cell during discharge. The electrode active materials are generally coated on metallic sheets, referred to as current collectors, that provide electronic connection to the external circuit. The electrodes are separated by a separator, which serves as both a physical barrier that is chemically and electrochemically inert, and a porous membrane that soaks up electrolyte.¹¹

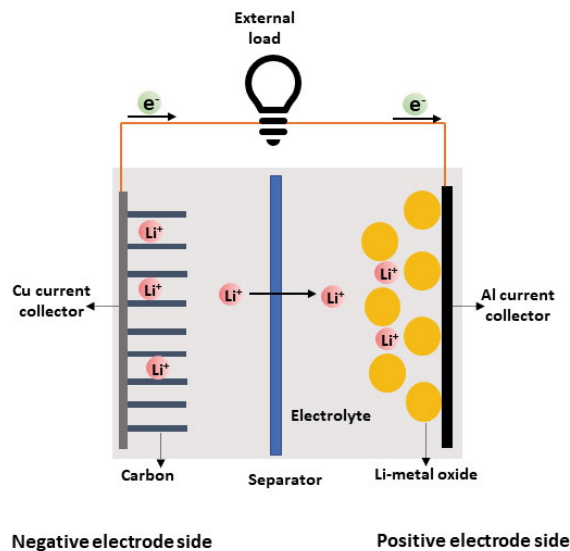


Figure 1.1: Schematic illustration of a Li-ion cell in operation. The electrodes are separated by a physical barrier, called separator. The ions diffuse from the negative to the positive electrode via the separator while electrons flow through an external circuit.

Upon several charge-discharge cycles, the performance of a Li-ion cell fades in terms of capacity loss and power. This is due to a large number of physical and (electro)chemical mechanisms, which affect the different components of the cells. Most of these ageing mechanisms are dominated by the surface processes occurring on either of the electrodes. It is therefore valuable to develop a deeper understanding of those processes that can have a detrimental effect on battery performance.

1.3 The LIB electrolyte

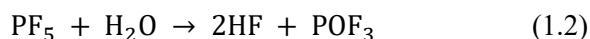
The state-of-the-art LIB electrolytes contain a Li-salt dissolved in a mixture of two or more organic carbonate-based solvents, with or without additive molecules. In his assessment, the scientist Kang Xu went into great length on what a perfect electrolyte should be and his conclusions were:⁷

- chemically inert towards electrodes, housing material and the separator.
- exhibit thermal stability.
- electrochemically stable over a wide voltage window.
- exhibit low viscosity.
- high ionically conductive over a wide range of temperatures.
- non-toxic, environment and cost-friendly.

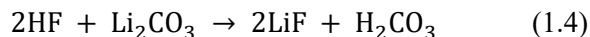
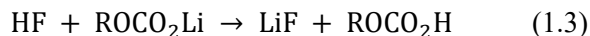
Typically, a mixture of more than one solvent in definite ratios is used in order to optimize the desirable properties of the electrolyte. On the other hand, only one electrolyte salt is commonly used because the interaction of more than one anion in the electrolyte salt can complicate the system and can add undesirable effects.

1.3.1 Lithium salts

The most common LIB electrolyte salt is the lithium hexafluorophosphate (LiPF_6). The salt permits high electrolyte conductivity combined with anodic stability up to 5.1 V vs. Li^+/Li . However, it is known to be hygroscopic and to react with residual water forming corrosive and highly reactive hydrogen fluoride (HF)¹² (reaction 1.1 and 1.2)



HF reacts readily with surface species such as carbonates (reaction 1.3 and 1.4)



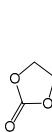
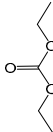
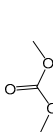
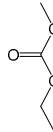
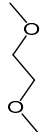
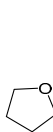

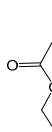
where R is a low-molecular-weight alkyl group. The primary reaction product resulting from these reactions is LiF. While LiF is recognized for its notable chemical stability,¹³ its presence in the cell remains a subject of debate. Some argue that it is an undesirable component in the cell due to its limited permeability for Li^+ ions.¹⁴ In addition to HF's reactivity towards carbonates, it can also favour dissolution of transition metals present in the positive electrode, which can then migrate and be reduced on the negative electrode surface.¹⁵

Some of the other Li-salts that have been widely studied are lithium perchlorate (LiClO_4), lithium bis(trifluoromethanesulfonyl)imide (LiTFSI) and lithium bis(oxalate)borate (LiBOB).¹⁶ Non-fluorinated LiClO_4 is known for its high conductivity and high solubility as well as high anodic stability, but imposes safety concerns at high temperature. Despite the disadvantages, LiClO_4 at a lab scale would be a good alternative to LiPF_6 to investigate interfacial reactions and avoid the interference of the reactive HF. Owing to the high stability of the perchlorate anion, it can be used in model studies and hence, is extensively used in this thesis.

1.3.2 Solvents

Most of the commonly used LIB solvents fall into the category of organic carbonates, esters and ethers (see Table 1.1).⁷ Carbonate solvents include linear and cyclic alkyl chained carbonates.

Table 1: Few of the commonly used LIB solvents with their physical properties¹⁷

Types	Solvent	Chemical structure	Molar mass (g/mol)	Density (g/cm ³)	Viscosity (25°C) (mPaS)	Tm/Tb (°C)	Dielectric constant
Carbonates	Ethylene carbonate, EC		88 .06	1.321	-	36/238	89.78
	Diethyl carbonate, DEC		118 .13	0.969	0.75	-74/126	2.80
	Dimethyl carbonate, DMC		90.08	1.063	0.59	5/91	3.10
	Ethyl methyl carbonate, EMC		104 .11	1.006	0.65	53/110	2.4
Ethers	Dimethoxyethane, DME		90.12	0.86	0.46	-58/85	7.2
	Tetrahydrofuran, THF		72.11	0.88	0.48	-108/66	7.4
	Diethyl ether		74.12	0.71	0.22	-116/34	
Esters	Ethyl acetate, EA		88.11	0.90	0.42	-83-77	5.9

Esters are known for their excellent anodic stability, but they are readily reduced at the negative electrode side making them unsuitable for operations at low potential. Carbonates, on the other hand, are known for their stability at potentials where most negative electrode materials operate. Ethylene carbonate (EC), one such carbonate solvent, is solid at room temperature but when mixed with a linear alkyl carbonate solvent, the mixture remains liquid over a wide range of temperatures. Although EC is viscous, its merit lies in the fact that it has high dielectric constant, and hence is able to dissolve salt in high concentration. During charge-discharge cycling, EC is known to decompose into both organic and inorganic compounds like lithium alkyl carbonates, alkoxides, oxalates, and various other lithium salts.^{18,19} These decomposition products may precipitate on the electrode surface and form surface film, which will be discussed extensively in the later section.

In this thesis, EC and a mixture of EC with DEC are extensively used as these are often used in the state-of-the-art LIBs and the objective is to combine the synergistic qualities of each solvent, namely the strong polarity of EC and the low viscosity of DEC, in the electrolyte. In addition to these carbonates, DME is also used as the background solvent in a study due to its superior chemical stability towards nucleophilic attack and also to avoid influence of other linear and cyclic carbonate.²⁰

1.3.3 Additives

Electrolyte additives are typically chemical species dissolved at low concentrations (<5 vol%) to improve electrolyte functions and cell performance.⁷ On the basis of their unique functionality, they can be classified into:

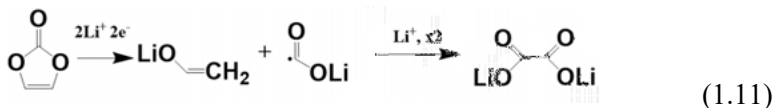
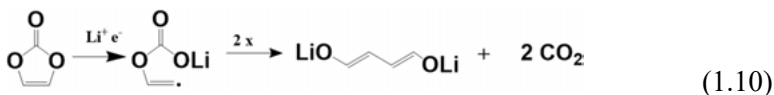
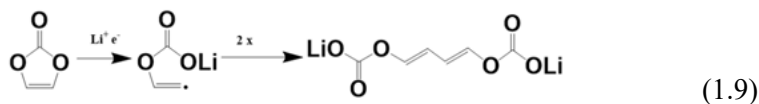
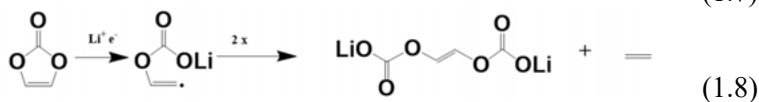
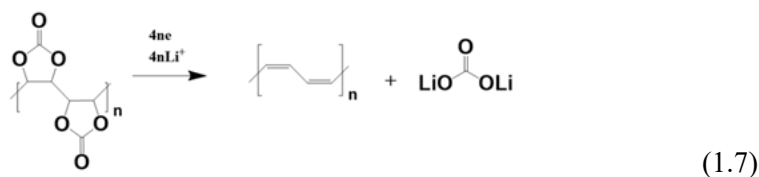
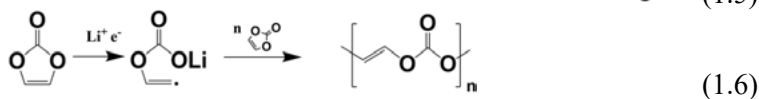
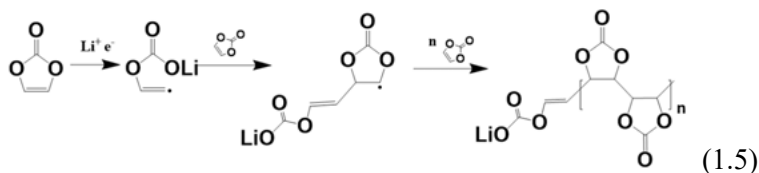
- Passivating layer formers (*e.g.*, vinylene carbonate (VC), fluoroethylene carbonate (FEC)),
- flame retardants (*e.g.*, hexamethoxycyclophosphazene (HMPN) and trimethyl phosphate (TMP)),
- cathode surface layer formers (*e.g.*, *n*-butylferrocene),
- ion conductivity enhancer (*e.g.*, boronates).

Comprehending the role played by electrolyte additives remains a significant challenge. For example, specific properties of the electrode passivation layer-forming additives responsible for achieving a more stable cycling lifetime, as well as the intricate details of the initial reduction processes governing the composition and morphology of the layer, are still not fully understood. Consequently, the assessment of whether surface layer-forming additive benefits cell performance relies on a laborious trial-and-error process through battery cycling.^{21,22} Additionally, extensive research efforts have been dedicated to computationally determine reduction voltages, enabling predictive screening of suitable additives for subsequent experimental testing.^{19,21}

1.3.3.1 Vinylene carbonate

VC was among the pioneering electrode passivation layer -forming additives that demonstrated genuine enhancement in LIB cycling stability, but its effectiveness relied on the appropriate dosage.²¹ Since the early 2000s, numerous advanced surface analysis techniques have been employed to investigate the composition of the nano-thick surface passivating layer generated by VC. Aurbach *et al.*²³ and Ota *et al.*²⁴ showed that the VC results into more flexible and cohesive polymeric species compared to when VC is absent in the electrolyte. The main polymeric species consisted of poly(VC), a ring-opened polymer of VC and polyacetylene. It was surmised that the presence of VC could help suppress both solvent and salt anion reduction, and therefore increase the thermal stability of the electrodes.

Efforts have been made to enhance our understanding of the mechanistic aspects related to various chemical reaction products and pathways for VC. The list of electro-chemical reactions of VC are (reactions 1.5-1.11):²⁴⁻²⁸



1.3.3.2 Tris(trimethylsilyl)phosphate

A large group of performance-enhancing additives contains organosilicon silyl groups (R_3Si , where R is methyl group), which when included are known to react with HF. Particularly, the silyl-functionalized phosphites ($P(OSiR_3)_3$) and phosphates ($O=P(O SiR_3)_3$) (as shown in Figure 1.2) have been researched for years.^{29–32} One well-known representative is tris(trimethylsilyl)phosphate (TMSPa), which, apart from scavenging HF, has also been claimed to be “multifunctional”, *e.g.*, in the sense of being an electrode layer former (both on the positive and negative electrode).^{31,33,34} The reactivity of this additive might not be restricted to only fluorides, but could also be extended to other chemical species which are present as cell constituents. In this thesis, TMSPa’s selective reactivity towards adverse chemical species has been utilized in order to disentangle the individual processes in the complex chemistry of a practical Li-ion cell.

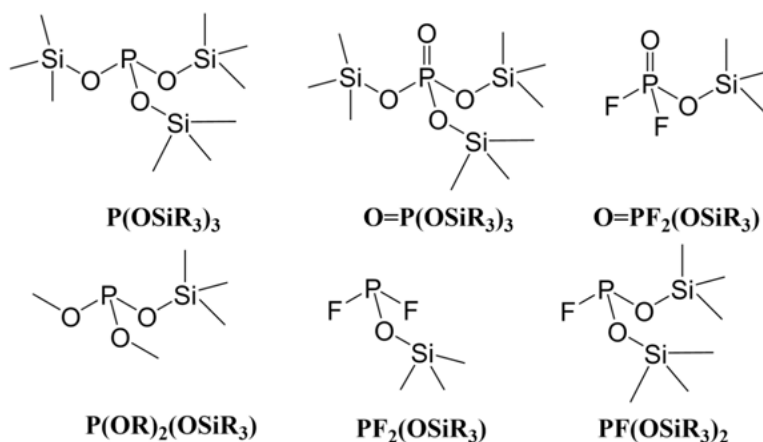


Figure 1.2: Examples of silyl functionalised electrolyte additives used in commercial LIBs. TMSPa is represented by $O=P(O SiR_3)_3$, where R denotes methyl group.

Indeed, it has been reported that $LiNi_{1/3}Mn_{1/3}Co_{1/3}O_2(NMC)/$ graphite-based Li-ion cells with TMSPa added display longer cycle and calendar life and exhibit lower impedance. Another study showed that TMSPa used as an additive in Li-rich NMC/graphite cells does not necessarily form a surface passivation layer by being electrochemically reduced/oxidized, as no gas evolution was registered in OEMS during reduction/oxidation. But they say that by scavenging other fluorides, such as LiF residues, TMSPa is able to lower the cell impedance.³⁵ Removing the highly resistive LiF from the surface layer while replacing it with side products from TMSPa degradation, such as P- and O-rich compounds, would increase Li^+ conductivity while at the same time suppress adverse side reactions within the cell.

1.4 Interfacial chemistry in LIBs

1.4.1 Interface and interphase

The interface marks the meeting point between the electrode and electrolyte. In classical electrochemistry, an ideal interface is conceptually two-dimensional, implying a negligible thickness. In order to fulfil this criterion, electrodes must operate within the electrochemical stability window (ESW) of the electrolyte. The ESW is the difference between oxidation and reduction potential of the electrolyte/electrode system. The oxidation potential of the electrolyte should be higher than that of the positive electrode while reduction potential of the electrolyte should ideally be lower than that of the negative electrode for the electrolyte to be electrochemically stable.³⁶

Simply put, an ideal interface must be clean *i.e.*, devoid of any “junks”. Failing to meet this criterion results in the interface between the electrode and electrolyte to transform into a distinct entity, provided the products forming this entity have lower solubility in order to precipitate and stay. This distinct entity is known as an “interphase”, a term introduced by Peled in 1979.³⁷

The interphase emerges from irreversible reactions between the electrode and electrolyte. These irreversible reactions render junction between the electrode and electrolyte no longer clean, as the solid “junk/residues” generated by the reactions deposit on the electrode surface, forming an independent three-dimensional phase.

On positive electrodes, the interphase layers are typically less discussed because positive electrode’s operational voltages often fall within the ESW. Consequently, fewer studies have been conducted on the interphase of positive electrodes. However, in recent years, there has been a growing recognition of the significance of these interphases, particularly in the context of high-voltage materials. The nomenclature for this interphase is hence less standardized, and terms such as the “solid permeable interface” or the “cathode electrolyte interphase” (CEI) have been employed.³⁸

In broad sense, interphase is just a special layer of products generated by the reactivity between electrode and electrolyte materials. An interphase can also be generated before any cell assembly, *e.g.*, Al_2O_3 coating on Al surface is also an interphase.

But before any interfacial chemistry takes place, a self-assembly of electrolyte solvent molecules driven by Li^+ mobility generates an interfacial electric double layer (EDL) between the electrolyte and electrode. The properties of these electrified interfaces control the chemistry and contribute to the overall performance of the electrochemical storage devices.

1.4.2 Electric double layer

Upon polarisation of the electrode negatively, charge (free electron) flows into the electrode. The charges entering the electrode reside at the surface and hence a gradient of charge is induced. Now, as a consequence, the solution side of the interface experiences a change in the potential. This leads to the redistribution of the charges (ions) in the electrolyte near the interface: the counter opposite charges of the same magnitude arrange themselves in the form of discrete layers closer to the interface boundary. One charge in a discrete layer exceeds the counter charge resulting in an excess or net charge density. The charge that is produced on the solution side of the phase boundary balances the charge of the metal side but in opposite polarity thus making the electrified interface or the EDL electrically neutral in nature.³⁹

The simplest interpretation, referred to as “*Helmholtz-Perrin parallel plate condenser model*” says that the variation of potential of the double layer with distance from the electrode into the solution is linear, similar to parallel plate capacitor.

Later, Gouy and Chapman came up with a model where they stated that the charges are rather free and not entirely restricted to the sheet. The charges are affected by the electric forces from the charges in the vicinity of the interface on the electrode side and hence the capacity is dependent on the potential. However, the model predicts the ions to be point charges and completely ignores the ion-ion interaction.

In practice, the complexity of an interface, particularly in the case of a liquid electrolyte arises from the distinct nature of the electrolyte. Unlike electrode materials, which often exhibit excellent electronic conductivity, the electrolyte comprises discrete ions solvated by solvent molecules. The random thermal motions of ions and solvent molecules disrupt the organized assembly of ions at the electrolyte-side interface. This disruption results in a diffuse ionic layer on the electrolyte side, causing a non-linear potential change across the interface.

The latest and most widely popular model is the *Bockris/Devanathan/Müller model*. It suggests that the solvent molecules (e.g., water) get adsorbed to the electrode surface and attain a fixed orientation towards the electrode surface (depending on its dipole moment) (Figure 1.3). The first layer of these dipolar solvent molecules together with specifically adsorbed ion displays a strong orientation to the electric field. This orientation has great influence on the dielectric constant of the bulk solvent that varies with applied field strength. The inner Helmholtz plane (IHP) passes through the centres of these specifically adsorbed and partially solvated ions. Outside of it lies the solvated ions of the electrolyte. The outer Helmholtz plane (OHP) passes through the centres of solvated ions.

As interfacial structure models are getting more and more aligned with reality, accurately describing the distributions of charge and potentials with

mathematical precision has become more challenging. To date, the *Helmholtz-Perrin Model* persists as the foundational and simplest model for theoretically elucidating interfaces.

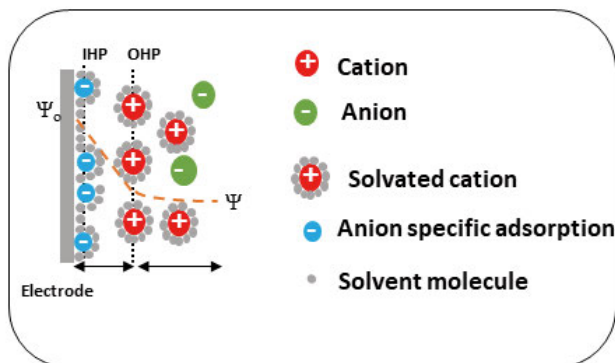
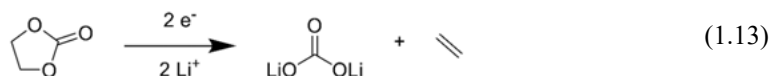
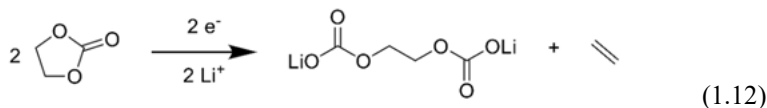


Figure 1.3: Schematic illustration of EDL according to the *Bockris/Devanathan/Mülken* model. The potential curve corresponding to the regions are presented with orange dotted line. These curves are useful as they indicate the strength of the electrical force between particles and the distance at which it operates.

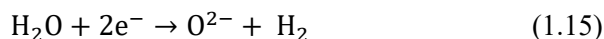
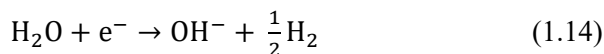
1.4.3 The solid electrolyte interphase-formation & ageing

In this term “solid electrolyte interphase”, SEI, the term “*solid*” signifies the layer's insolubility, “*electrolyte*” denotes its ion-conducting and electron-insulating characteristics and “*interphase*” indicates its status as an autonomous phase situated between the electrode and electrolyte, possessing a distinct thickness, chemical composition, and morphology. For a typical $\text{LiCoO}_2/\text{graphite}$ full cell, LiCoO_2 is within the ESW, while graphite is not. According to the general consensus, for graphite, reduction of electrolyte starts around 0.8 V vs. Li^+/Li , thus making graphite a site for electrolyte reduction. The direct EC (one of the most important ingredients of the electrolyte) reduction by one-electron and two-electrons pathway results in lithium alkyl carbonates (reaction 1.12) and lithium carbonates (reaction 1.13), respectively, with the evolution of alkene gases.⁴⁰

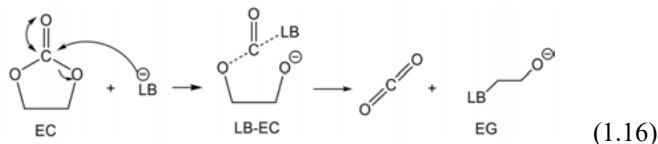


Depending on their respective solubilities, they may precipitate on the electrode surface to form the SEI.

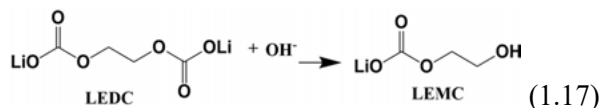
Water is always brought in to cell with every cell component because of the difficulty to perfectly dry these components. As a result, the water content in the cell can easily reach up to hundreds of ppm. During the initial polarization process, this trace water can be reduced, forming Lewis bases (LBs) like lithium hydroxide and lithium oxide (reaction 1.14 and 1.15)



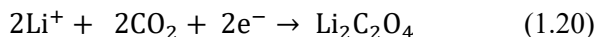
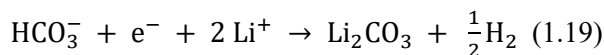
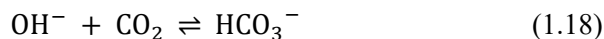
OH^- that are generated at the negative electrode side creates a basic environment which further leads to parasitic side reactions. For example, EC can decompose to produce CO_2 and glycols (reaction 1.16)



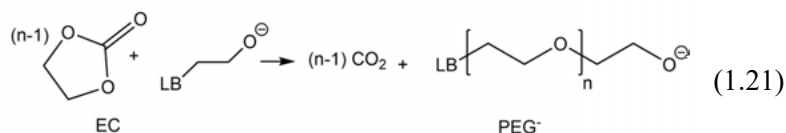
The OH^- can also react with LEDC to form lithium ethyl monocarbonate (LEMC)⁴¹ (reaction 1.17)



CO_2 which is generated in the cell can react with OH^- to form bicarbonates, carbonates and oxalates (reaction 1.18, 1.19 and 1.20)



Furthermore, EC is also known to polymerise at elevated temperature forming poly-(ethylene-oxide/glycols) (PEO)/(PEG)-like polymers^{42,43} (reaction 1.21) which either deposit on the active materials or dissolve in the electrolyte resulting in increased cell impedance.⁴⁴



The polymerisation reaction of EC is accompanied by evolution of CO₂ (as described above) which again plays an important role in SEI composition. The formation of these polymers on the electrode surface is a somewhat more controversial issue, since firstly, the exact role of these species is still unknown in batteries and secondly, they have been difficult to identify with standard spectroscopic techniques.

An ideal well-formed SEI is chemically stable, non-dissolving, and prevents further solvent degradation while still allowing for sufficient Li⁺ transport between the electrolyte and electrode during dis-/charge. The composition, structure and formation mechanism of the SEI is still under debate despite numerous studies performed over last three decades.⁴⁵ According to the first SEI model presented in 1979³⁷, and further developed in 1983 by Peled⁴⁶, the SEI consists of two layers: a compact thin inner layer and a porous outer layer. A simple illustration of this model is presented in Figure 1.4. In 1995, Aurbach *et al.* further proposed that the inner layer consists of inorganic species, such as LiF and Li₂O, while the outer layer consists of organic species such as lithium alkyl carbonates (illustrated in Figure 1.4).⁴⁷ Furthermore in 1997, Peled modified their previous model and proposed a ‘mosaic structured’, ‘polyhetero’ microphase model where different species are in the form of microregions and arranged in the order in which the electrolyte constituents are reduced.⁴⁸ Later in 1999, Ein-Eli suggested another SEI model in which the decomposed electrolyte solvents adheres to the negatively charged graphite surface through coulombic interaction.⁴⁹ Recent models suggest that the SEI formed on graphite consists of an inner inorganic matrix and a porous outer organic layer.^{50,51} They reported LiF crystals on the SEI. Thus, one thing is certain: having a functional SEI is very important for the proper functioning of the cell. Understanding the underlying formation mechanism could help us understand our existing system better and design better batteries for future. Hence, the thesis explores into this very field and seeks answer to the question “*what does the solid electrolyte interphase constitute and what are the various chemical and electrochemical reactions involved during its formation?*”.

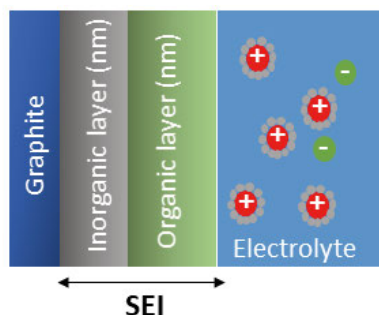


Figure 1.4: Schematic illustration of SEI model in the lithium-ion battery

1.5 Characterisation techniques for interphases

A widespread set of methodologies are used to analyse the SEI on the electrode. Ever since, *ex-situ* measurements with X-ray photoelectron spectroscopy (XPS) and vibrational spectroscopy such as Fourier transformation Infrared (FTIR) and Raman spectroscopy are employed to probe the electrode surface after cycling.⁵² However, the downside of *ex-situ* techniques is that it involves sample preparation steps which could modify the SEI (as SEI is extremely thin and sensitive to atmosphere), as a result of which valuable information is lost. To circumvent this issue, concerted efforts have been made to develop *in-situ* technique, under environments mimicking those encountered during cycling, or better yet *operando* mode, that enables monitoring the changes as the reactions take place during operation, thus giving information about the decomposition of the electrolyte. Furthermore, many additional decomposition reactions and products can be predicted based on *ab initio* calculations.

A few of the techniques employed in this thesis are described in this section. A significant part of the PhD work deals with the development of the *operando* Raman spectroscopy cell set-up and hence, in this thesis, this technique is explained in greater detail.

1.6 Raman spectroscopy

1.6.1 Principles of Raman spectroscopy

When monochromatic radiation is passed through a medium, most of the light is transmitted without any change, while a minor fraction gets scattered. If the scattered light is analysed by means of a spectrometer, light is found to undergo both elastic and inelastic scattering.⁵³ When light is elastically scattered, it is called Rayleigh scattering, while the inelastically scattered light is

known as Raman scattering and the phenomenon is called ‘Raman effect’ (Figure 1.5). The spontaneous Raman effect takes place when the molecule under study absorbs incoming radiation and is excited from the ground state to a “virtual” energy state, thereafter they relax into a vibrational excited state, giving Stokes line. On the other hand, anti-Stokes lines occur when the valence electrons of the molecule are already in the excited vibration state. Normally only the Stokes part of the entire spectrum is measured, since it is more intense than the anti-Stokes part. Raman scattering leads to a change in vibrational energy of a molecule (stretching and bending of bonds) and hence it is termed as ‘vibrational spectroscopy’. In contrast to infrared absorption, which is another form of vibrational spectroscopy utilizing the change in electric dipole moment of the molecule, Raman scattering spectroscopy is a result of the molecule undergoing a change in electronic polarizability.

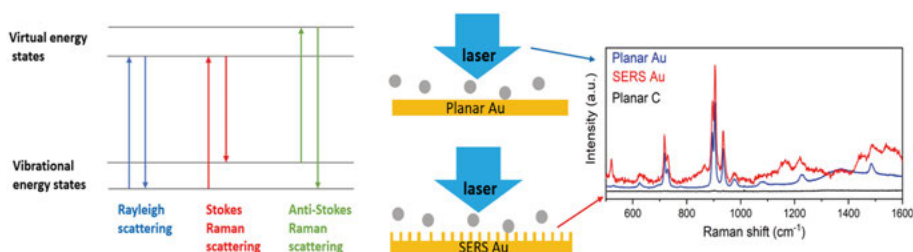


Figure 1.5: On left, principle of classical Raman effect is schematically represented. On right, spectra obtained from classical Raman (on planar Au) and SERS (on nanostructured Au) are shown.

Approximately only 1 in 10^7 photons is scattered inelastically. This low count of photons results in a weak Raman signal and therefore it displays a low sensitivity. However, Raman scattering can be locally enhanced in the vicinity of nanostructured coinage metals, a strategy denoted surface-enhanced Raman spectroscopy (SERS, Figure 1.5, on right)

1.6.2 Surface-enhanced Raman spectroscopy

SERS enables detection of even single molecules when placed in close proximity to nanostructured metal surface. The exact mechanism behind such a signal enhancement from the adsorbates has not yet been conclusively determined. Two of the most widely accepted theories are:⁵⁴⁻⁵⁶ 1) *Electromagnetic*: When light is incident on the metallic surface, localized surface plasmons are excited. When the frequency of the oscillating electric field of the incident light is in resonance with that of the surface plasmons, enhancement of the electric field near the surface occurs which magnifies the intensity of the Raman scattering light. The word “localized” means that the electron oscillations

do not propagate, but are spatially localized in three dimensions typically smaller than the wavelength of light. The field enhancement occurs at two instances. First, the field enhancement due to local surface plasmon resonance (LSPR) at the interface magnifies the intensity of incident light, which will excite the Raman modes of the molecule being studied, therefore increasing the signal of the Raman scattering. The Raman signal of the scattering light is then further magnified by the surface due to the same mechanism that excited the incident light, resulting in a greater increase in the total output. 2) *Chemical*: Upon interaction with the incident light, the metallic substrate alters the distribution of charges within adsorbate molecules, resulting in a greater polarizability, hence, causing a stronger Raman scattering. Although the chemical effect leads to a relatively weaker enhancement as compared to the electromagnetic mechanism, it is mostly responsible for the determination of frequency shift and relative intensity of the peaks, in electrochemical systems.⁵⁴ One of the two main factors influencing the surface-enhancement is substrate type and its morphology. Generally, Au, Ag and Cu are known to exhibit SERS activity owing to the optical properties of the free electrons sustaining the surface plasmon resonance. Although SERS can be observed from electric field enhancement at single nanoparticle or a very sharp tip, it is beneficial to have tailored nanostructures, *e.g.*, allowing the analyte molecules to be placed within nano-gaps between two metal particles, or between the particle and the surface. These nanometer-sized spatial regions are called “hotspots” which can lead to enhancement factors (EF) of about 10^5 - 10^6 (will be discussed in details in the section 4.1.1). The second factor is excitation wavelength. The laser excitation wavelength influences the Raman band intensity since the radiated power by an oscillating dipole is inversely proportional to the fourth power of the laser wavelength ($I \sim \lambda^{-4}$). This means that the same molecule scatters more Raman photons when excited with green laser light (532 nm) than when excited with near-infrared light (785 nm). However, since the cross section for fluorescence is larger (about 6 to 10 orders of magnitude) than Raman scattering, Raman spectra might get overwhelmed by the fluorescence background making the detection of Raman spectroscopic signatures, even when surface enhanced, extremely difficult. The source of fluorescence is typically from the fluorescent impurities, even in trace amounts, or defects within the crystal lattice arrangement or exciton-coulomb related electron-hole pair.

1.6.3 State-of-the-art SERS studies on interphases

SERS has been employed for *in-situ* and *operando* studies of SEI formation due to the high intrinsic surface sensitivity, simple set-up, and commercially available optimized SERS substrates. Sang-Don Han *et al.* employed *in-situ* SERS to study the composition of the SEI on a silicon negative electrode and correlated the spectroscopic observations with the electrochemical perfor-

mance of the electrode.⁵⁷ They detected lithium carboxylate and lithium propionate species in the SEI formed in EC:EMC based electrolyte. Mozhzhukhina *et al.* showed that when a model Au SERS substrate is negatively polarized, charging of the electric double layer appears to be directly observed until the formation of SEI, which subsequently dominates the spectral response.⁵⁸ The *operando* methodology showed that electrolyte impurities, such as HF and H₂O, even if present in trace amounts, significantly contribute to the SEI dominated by LiF and Li₂CO₃ formed in multistep (electro-)chemical processes. Further more advanced Raman spectroscopy substrates include the shell-isolated nanoparticle-enhanced Raman spectroscopy (SHINERS), first employed by Hy *et al.* to investigate the SEI formation on Si and Cu electrodes.⁵⁹ They reported the presence of VC reduction product in the SEI when cycled with VC containing electrolyte. Recently, Gajan *et al.* employed the SHINERS approach under *operando* conditions to track the dynamic evolution of the SEI on Au and Sn electrodes upon cycling of LIB cells.⁶⁰ They were able to detect diethyl 2,5-dioxahexane dicarboxylate (DEDOHC) compound in the SEI formed on Sn but not on Au negative electrode, thus highlighting the catalytic effect of the tin oxide (SnO₂) substrate electrode towards reactions with DEC and EC. Classical experimental challenges commonly found in the field of surface science, such as influence of impurities, were however not addressed.

1.7 Nuclear Magnetic Resonance

Nuclear magnetic resonance (NMR) is a spectroscopic technique commonly utilized to analyse the molecular structure of a compound by observing and measuring the interactions of its atomic nuclear spins. Nuclear spins line up in one direction under the influence of an external magnetic field, when the atomic nuclei are exposed to a radiofrequency pulse, the spins flip to a higher energy state. As the spin relax back to the lower spin state, it emits energy which is equivalent to an energy value characteristic of the nucleus type and environment. The primary parameter to take into account is the angular momentum caused by the spin of the magnetically active atomic nuclei (gyromagnetic ratio, $\gamma \neq 0$). From a classical perspective, the magnetisation axis spins over the direction of B_0 (static magnetic field) with a characteristic Larmour frequency (ω_0), defined as $\omega_0 = \gamma B_0$. 2D NMR experiments are related to NMR spectra with two orthogonal frequency axes and they can be classified as homonuclear or heteronuclear NMR experiments. 2D homonuclear NMR experiments display the same nuclei (*e.g.*, ¹H-¹H or ¹³C-¹³C) on the two different frequency axes of the 2D spectrum. 2D heteronuclear NMR experiments display information about two different nuclei on the two orthogonal axes of a 2D spectrum. For instance, in proton-detected experiments such as

the classical heteronuclear single quantum correlation (HSQC) or heteronuclear multiple bond correlation (HMBC) experiments, the ^1H nucleus frequency information is usually displayed on the F2 dimension (horizontal axis) and ^{13}C nuclei are shown onto the indirect F1 dimension (vertical axis). The HMBC spectra give correlations between carbons and protons that are separated by two, three, and, sometimes in conjugated systems, even four bonds. The HSQC spectra give correlation between carbons and protons that are directly bonded to each other (single-bond correlations).

In general, nuclei typically exhibit NMR signals associated with the local chemical environments, influencing characteristics such as the chemical shifts, signal peak shape *etc.* Therefore, NMR spectroscopy allows these species to be distinguished on a local atomic level. In the field of batteries, this technique is useful to characterise electrolyte decomposition products that are produced under various cell operating conditions and thus, one could infer the primary reaction involved during the process.^{61–63} It is often very suitable for the study of complicated mixtures with components that are present in low concentrations. In this thesis, solution NMR is employed to identify the reaction products that are present in liquid phase.

1.8 Online Electrochemical Mass spectrometry

Mass spectrometry (MS) is used to qualitatively and quantitatively probe the volatile gaseous products. A highly successful and promising approach is online electrochemical MS (OEMS) developed for the study of electrode potential-induced reactions.⁶⁴ The set-up consists of an electrochemical cell, a gas sampling system, and a capillary inlet to the MS.⁶⁴ Gas that is present or generated in the cell is sampled out during operation and injected into the MS. When the gaseous molecules enter the mass spectrometer, they are ionized by an ionisation source present in the spectrometer and then the ionised molecules and possible fragments thereof are accelerated into a mass filter, which separates gaseous molecules according to their mass (m) and charge (z).

A few of the volatile reaction products relevant to this thesis with their corresponding m/z channels are: H_2 -2, H_2O -18, methane-15,16, ethane- 26, 28, 30, methanol-31, ethanol- 31, 45, 46, C_2H_4 -26, O_2 -32, CO_2 -44, POF_3 - 85 and DEC- 91.^{64,65}

By probing the gaseous phase of the cell, OEMS offers several advantages, including significantly reduced electrolyte-induced background in the MS and enhanced sensitivity for detecting various reaction products. This capability is crucial for gaining insights into electrochemical processes and understanding their underlying mechanisms.

2 Thesis scope

The thesis explores primarily chemical and electrochemical reaction pathways of electrolytes at the negative electrode of a Li-ion cell. A practical LIB is a multi-composite system that involves a complex chemistry of SEI layer formation. Several details of experimental conditions, such as electrode substrate composition/morphology, electrolyte volume per surface area and purity, *etc.*, often lead to complicated results, thus making the analysis challenging. Hence, in this thesis, model systems are employed in order to reduce complexity. By reducing the number of components, *e.g.*, by introducing a more well-defined single-element surface and simplified electrolytes, the likelihood of unpredictable side-reactions is lower and the possibility of tracing the reaction products increases, thus facilitating spectral deconvolution and analysis. In **paper I**, the real-time formation of SEI is comprehensively investigated using *operando* surface enhanced Raman spectroscopy. By negatively polarizing the Au SERS substrate in a half cell configuration down to 0.5 V vs. Li^+/Li (where SEI is expected to have formed) in a model electrolyte, the influence of the individual electrolyte constituents, including impurities in the cell, is summarised. Complementary to Raman analysis, OEMS is utilized to characterise volatile gaseous products evolved during the SEI formation on the Au substrate immersed in an EC-based single solvent electrolyte. Implementing these measurements on solid/liquid LIB interfaces requires a sophisticated experimental setup. Therefore, practical aspects have been discussed, such as the choice of an appropriate SERS substrate, the configuration of an electrochemical setup, and the formulation of the measurement procedure.

It is not necessary that all the electrolyte decomposition leading to SEI take place via electrochemical processes or involve a reduction step; some decompositions occur through thermally activated chemical reactions. For example, chemical hydrolysis of EC forms CO_2 . The reduced negative electrode establishes a highly alkaline environment, further contributing to these side-reactions. Hence in the follow-up studies, the focus is placed on mechanistic understanding of the chemical degradation reactions of different electrolyte components (solvents and additive) in presence of LBs typically found in LIBs. The degradation process of VC, a commonly used SEI-forming additive, has been overlooked in many studies because it shows up at the H_2O reduction potential and assumed to be purely electrochemical. Understanding its chemical degradation is very important to understand its effect and realise the full

potential of such an additive. Thus, the chemical degradation processes of VC and kinetics of its hydrolysis are studied in great detail and compared with its saturated counterpart, EC (in **paper II**). The experimental results include a combination of gas analysis and solution NMR spectroscopic analysis. In **Paper III**, light was shed on the electrochemical reduction reaction pathways of VC on carbon electrode by *operando* gas analysis. A new understanding of the VC electrochemical reduction processes and hydrolysis as well as their possible positive influence on SEI formation processes is highlighted.

The thesis at later stage (**paper IV**) proceeds with an investigation to uncover the reactivity of the LBs towards TMSPa, a representative of the commonly used silyl derivative phosphate electrolyte additive family. This is an attempt to describe the dynamic nature of the SEI and use the electrolyte additive as chemical probe to perform the reaction mechanistic study. NMR and *in-situ* injection cell-coupled MS are employed to detect and identify the reaction products. In **Paper V**, the previous study (**Paper IV**) was expanded upon, delving deeper to gain insights into the reactivities of TMSPa towards H₂O in LIBs. Although the detrimental impact of H₂O impurities on the performance of Li-ion cells is widely acknowledged, the specific reaction pathway of H₂O in real cells has received limited investigation and understanding. Based on the evidence from NMR and GCMS analysis complemented by molecular dynamics-density functional theory (MD-DFT) simulations, a new reaction pathway is proposed. Thus, at the end of **Paper IV** and **V**, a new understanding of the additive reaction mechanism is attained.

3 Experimental

The electrolyte solutions used in the experiments were prepared as per the procedures stated in **paper I, II, III, IV and V** respectively. The solution storage, sample preparation and cell assembly were done in the glovebox and the H₂O and O₂ contents inside it were kept below 1 ppm.

3.1 SERS

The *operando* Raman measurement (Renishaw InVia 2013 spectrometer, UK) in **paper I** was performed in a custom-made spectro-electrochemical cell where SERS Au (company Silmeco, Denmark)⁶⁶ is used as the model working electrode. The SERS-active substrate measures $\sim 3 \times 3$ mm and features free-standing Si nanopillars, all of uniform height (~ 1000 nm), capped with a layer of Au. Refer to Figure 3.1(a) and (b) for scanning electron microscope images of the substrate.

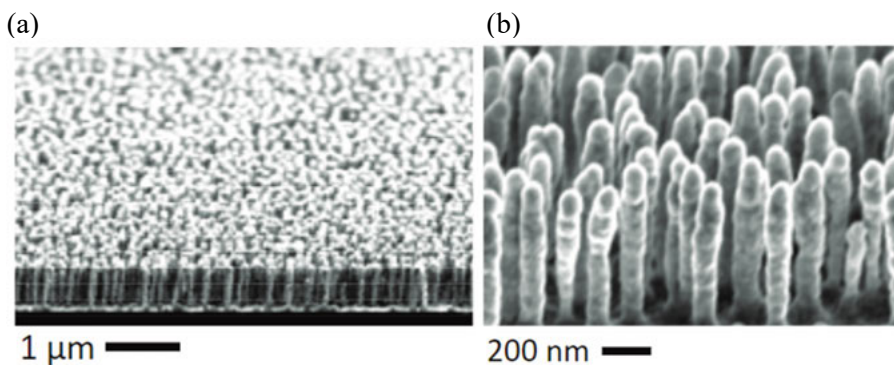
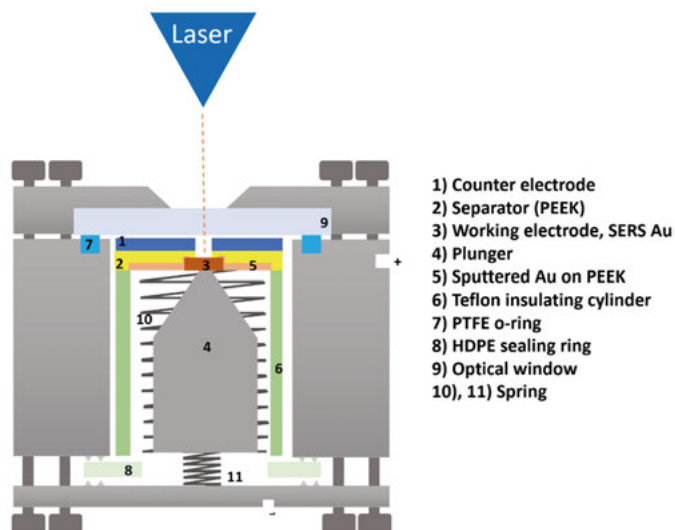


Figure 3.1: (a) and (b): SEM images of the SERS-active substrate used in this thesis. The nanopillars across large areas have a uniform height.⁶⁶ Copyright (2012) Wiley.

A schematic illustration of the custom-made spectro-electrochemical cell is presented in Figure 3.2(a)). A lithium foil is used as a counter electrode and 50 μL of a model electrolyte based on only a single salt in single solvent *i.e.*, LiClO₄ in EC mixed in 1:6 molar ratio. The Li foil was pierced in the middle of 1 mm diameter hole. The laser beam impinges the Au substrate through the hole in the Li and the electrolyte.

(a)



(b)

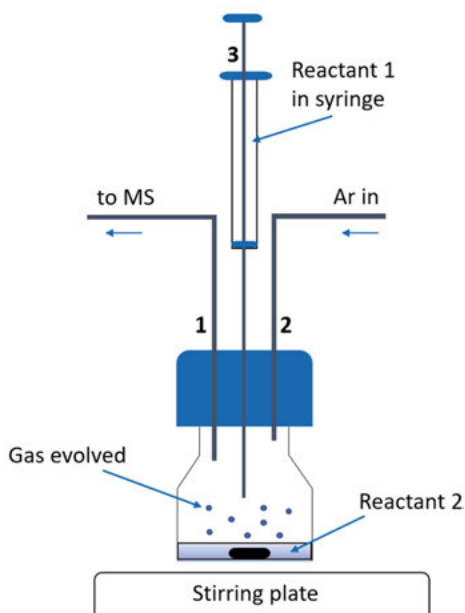


Figure 3.2: Schematic illustration of the (a) *operando* Raman cell and (b) injection cell set-up used in this thesis.

The Raman spectra were obtained with a laser power source of wavelength of 785 nm (laser power 1.5 mW) and grating of 1200 lines/mm. The acquisition

time for one Raman spectrum was 100 s (20 s * 5 accumulations). The standard mode laser spot size is $\sim 1.5\ \mu\text{m}$ at 50x magnification. Raman spectroscopy was performed during the same time as reducing the electrolyte on the Au. Autofluorescence background was corrected and the peak fitting was performed using least-square minimization of Lorentzian type peaks in a custom-made python-script.

3.2 NMR

In **paper II**, VC was exposed to water in presence of a LB, namely hydrated tetrabutylammonium hydroxide in certain molar ratio. Anhydrous dimethylsulfoxide (DMSO)- d_6 (99.9%, VWR) was taken as the background solvent and internal standard for ^1H (2.46 ppm) and ^{13}C (39.9 ppm) for NMR. In **paper III**, 120 μL of electrolytes were extracted from cycled cells and put into the outer tube and the inner coaxial tube was filled with the deuterated solvent. In **paper IV**, saturated LB solutions were prepared by adding 100 mg of LBs in 2 mL of EC:DEC(1:1 v/v) mixture in separate vials. In **paper V**, similar sample preparation procedure was undertaken, where 0.5 to 5v% H_2O was added to the background solvent. For samples with the additive, 5v% TMSPa was added to the solution. ^1H , 400 and 600 MHz; ^{13}C , 162 MHz; ^{31}P , 162 MHz; ^{19}F , 376 MHz NMR spectrometer (JEOL, 400 MHz and Bruker, 600 MHz) were used, and chemical shifts were recorded in parts per million (ppm). All spectra were processed and analysed by MestReNova 6.0.2-5475.

3.3 Mass spectrometry

In **paper I, II and III**, OEMS is employed which is able to monitor the gases evolved during the cell operation and hence deduce the chemical reactions responsible for those products. In **paper II** again and in **paper IV**, a slightly different set-up of MS is used where the MS is coupled to a vial/chamber with a syringe that allows a qualitative and quantitative analysis of the various gases evolved as a result of the chemical reaction taking place therein upon injection of the content into the reactive chamber (illustration of the set-up in Figure 3.2 (b)).

1.1.1. OEMS cell assembly

As stated in **paper I**, in OEMS cell, circular Au-coated stainless-steel mesh electrodes were used as working electrode. To avoid gas evolution from the counter electrode, LiFePO_4 electrodes were punched and delithiated to 3.43 V vs. Li^+/Li before assembly. Linear sweep voltammetry (LSV) was performed from open circuit potential (OCP) down to 0.5 V vs. Li^+/Li with a scan rate of

0.1 mV s⁻¹. In **paper II and III**, the same procedure was done, glassy carbon electrode was taken as negative electrode, the baseline electrolyte was replaced with LP40 in paper II and LiClO₄ in DME in paper III.

3.3.1 Injection cell set-up

The gas analysis setup (as shown in figure 3.1 (b)) consists of a custom-made injection cell, which is a blue-capped bottle of 10 mL volume (Duran Glas, Sweden). The lid of the bottle has three connections: (1) an outlet to periodically sample the evolved gases to the mass spectrometer (PrismaPlus QME220), (2) an inlet to refill the cell with fresh Ar gas, and (3) a syringe for injection. The temperature and pressure in the cell are monitored using a high precision transducer (Keller-Druck GmbH, Switzerland). The sampling system and the cell are integrated inside a temperature-controlled incubator chamber (Tritec, Germany).

The time between each sampling point was set to 180 s, and an initial baseline was performed until there was a stable background signal. Once a stable background is achieved, reactants from the syringe were mixed with the reactants in the vial and periodic sampling was done as stated previously. The solution was magnetically stirred to ensure a homogeneous mixing. In **paper II**, the gas evolution rate was presented in $\mu\text{mol}/\text{min}$. In **paper IV**, the partial pressure of gas species in Ar flow is documented as normalized ion current, with respect to Ar and surface area of the LB powder. Each gas species is recorded at a relevant mass-to-charge ratio (m/z): H₂-2, O₂-32, Ar-36, CO₂-44, TMSPa-73, TMSOH-75, TMSF-77, TMSOCH₃-89, and DEC-91. The gas profiles for each experiment were compared with its blank, *i.e.*, EC:DEC mixture only (without any LB). For the experiments with additives, the gas evolved was compared with blank samples without additives.

3.4 Other characterisation techniques

3.4.1 Gas chromatography mass spectrometry

The experiments with liquid injections were done with an injection volume of 0.1 μL . The GCMS measurements were done with a Shimadzu GCMS equipped with stand-alone auto injector and GC capillary. Helium was used as carrier gas. The temperature program started at 100 °C which was held for 1 min. The temperature was ramped with 30 °C min⁻¹ until 280 °C and held at 280 °C for 1 min. The overall measurement time was 11 min with a mass range from 25–700 m/z . The mass spectrometer was run in the electron impact ionization (EI) mode with the following parameters: the temperature of the ion source was set to 220 °C; the inter-face was held at 250 °C and the filament was operated at a voltage of 70 V; the detector voltage was set relative to the

respective tuning results. The values presented in this work are reported as relative intensity with respect to the highest peak in the specific measurement, i.e., the DEC peak.

3.4.2 Coulometric Karl-Fischer titration

To determine the amount of water consumed during VC decomposition, a series of electrolyte mixtures were prepared and tested with coulometric Karl-Fischer titrator. DME was taken as the background solvent. The first series of electrolyte mixture was prepared by deliberately contaminating the DME with 667 ppm of H_2O . To that mixture, VC added such that overall DME:VC=99:1 v/v is obtained.

The second series of electrolyte was prepared by adding TBAOH.30 H_2O in DME. The concentrations of TBAOH.30 H_2O were adjusted to achieve the same H_2O concentrations in the electrolyte as in the H_2O -containing electrolytes. To the DME+ TBAOH.30 H_2O mixture, VC was added such that overall DME:VC is 99:1 v/v.

Similar procedure was followed to prepare an electrolyte solution where VC was replaced with EC.

4 Summary of key results and discussion

In this chapter, the key findings related to chemical and electrochemical reactions during interphase formation using model systems are presented.

In section 4.1 (based on **paper I**), the role of electrolyte constituents, including impurities in the SEI build-up is presented based on advanced *operando* investigation.

In section 4.2.1 (based on **paper II and III**), kinetics of VC hydrolysis and electrochemical reduction pathways of VC are presented, and the resulting products from VC decomposition reaction are thoroughly discussed.

In section 4.2.2 (based on **paper IV and V**), the reactivity of commonly found LBs in LIB with TMSPa and the fate of the resulting products from their reactions are presented.

4.1 Advanced *operando* investigation of interphase formation

In **paper I**, *operando* Raman spectroscopy and complimentary OEMS were employed to study the SEI formation on SERS-active Au in a model electrolyte based on LiClO₄ in EC. The results show that SEI formation mechanism is triggered by several electro-/chemical processes. In addition to that, the limitations and challenges of this advanced spectroscopic technique are also addressed.

4.1.1 Determination of the SERS enhancement factor

The SERS enhancement factor is a measure of the SERS effect, and hence the performance of various substrates. Typically, an average EF reported in literature is of the order of $\sim 10^5$ - 10^6 , sometimes as high as $\sim 10^{14}$ are also encountered, which is sufficient for the observation of single molecule SERS signals.⁵⁵ Accurate experimental determination of single molecule enhancement factor is however challenging and a direct comparison between various literature sources is not so straight forward as it greatly depends upon the measurement conditions and procedures: substrate type, analyte molecule, excitation wavelength *etc.*

Generally, the SERS EF is determined with the formula

$$EF = \frac{\frac{I_{SERS}}{N_{SERS}}}{\frac{I_{RS}}{N_{RS}}} \quad (4.1)$$

where, I_{SERS} and I_{RS} are the intensities of the characteristic band in the SERS spectrum and normal Raman (non-SERS) spectrum, respectively and N_{SERS} and N_{RS} are the number of molecules probed in SERS and normal Raman respectively.

In order to determine the EF of our substrate, the commonly employed 1mM rhodamine 6G (Rh6G) in ethanol solution was taken as the analyte solution. Figure 4.1(a) and (b) show SERS and normal Raman spectra recorded under identical experimental conditions (785 nm laser wavelength, 10mW laser power, 50x microscope objective lenses) and for the same sample preparation conditions. I_{SERS} and I_{RS} are determined from the strongest signal at 1512 cm^{-1} characteristic to aromatic C–C stretching of the Rh6G molecule (figure 4.1 (c)). The EF is found to be 5.3×10^4 for our substrate.

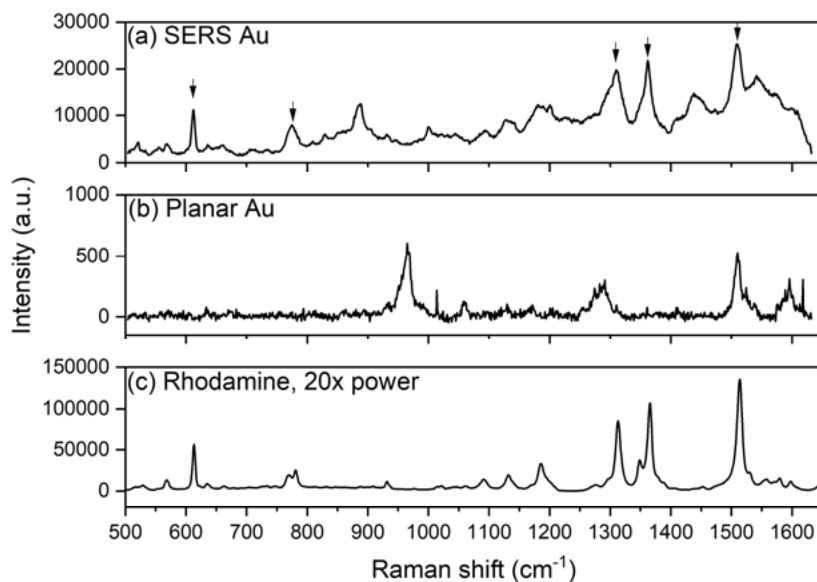


Figure 4.1: Raman spectra recorded for Rh6G analyte on (a) SERS Au, (b) Non-SERS Au under same conditions, and (c) Pure compound, raised to 20 times the power used for the other measurements.

The extent to which SERS signal from the Rh6G is enhanced by the SERS Au surface appears to be low ($<10^6$ commonly encountered) compared to planar Au. Possibly, the planar Au also maintains a certain enhancement effect (*e.g.*, from nano-roughness on its surface), hence rendering an immediate comparison between the two substrates unfair. Nevertheless, a SERS effect is observed

and the Raman signal from Li-ion electrolytes is expected to be enhanced when in contact with the substrate.

4.1.2 Electrochemistry

OEMS and *operando* Raman half cells were assembled and the current response from the Au-based working electrodes during the first cathodic potential sweep (at 0.1 mVs^{-1} scan rate) from OCP vs. Li^+/Li to $0.5 \text{ V vs. Li}^+/\text{Li}$ was recorded. $\text{LiClO}_4\text{:EC}$ (1:6 molar ratio) was taken as the model electrolyte, as mentioned in previous section. As can be observed in Figure 4.2 (as also in **paper I**), the current profiles differ for the two systems, which is attributed to the variation in the two cell designs and geometries. However, the main common observations are reduction peaks starting at 2.0 V , 1.6 V , and 1.0 V , all of which can be assigned to unique gas evolution processes, as will be discussed in the following section 4.1.3.

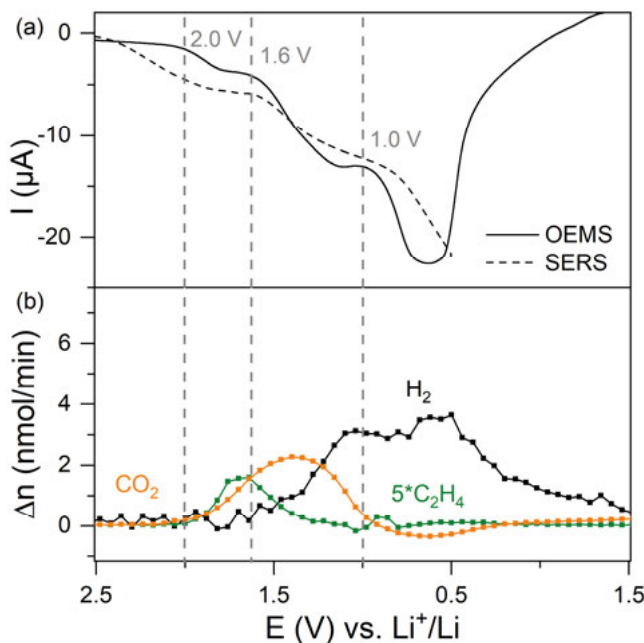


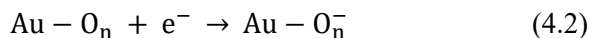
Figure 4.2: (a) Current response, I , of an Au working electrode in the OEMS cell and an Au SERS substrate in the *operando* Raman cell (b) Gas evolution rate, Δn , of the main gases (orange CO_2 , green C_2H_4 and black H_2) evolved presented in nmol/min. Reprinted with permission from reference.¹

4.1.3 Investigating the gas evolution

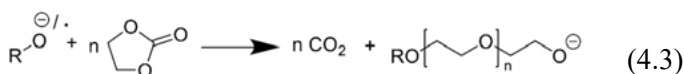
The first process starting at 2.0 V is associated with the evolution of ethylene (C_2H_4) (Figure 4.2). This process is assigned to EC reduction caused by a two-

electron reduction pathway (reaction 1.13) that results into the formation of lithium carbonate (Li_2CO_3) and C_2H_4 .

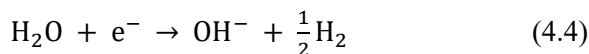
CO_2 is however observed to evolve roughly at the same time and is believed to derive from the ring-opening process of EC induced by the reduction of oxygen impurities. Previous studies on Li-air batteries with organic carbonate-based electrolytes have shown that oxygen reduction ($E_{\text{ORR}} \sim 2.5\text{-}3.0 \text{ V vs. Li}^+/\text{Li}$) leads to the formation of superoxides (reaction 4.2)



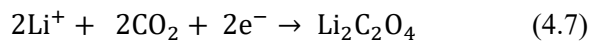
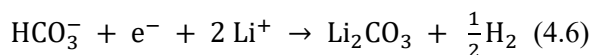
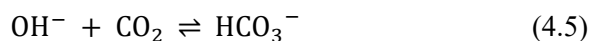
that can chemically ring-open EC through a nucleophilic reaction.⁶⁷⁻⁶⁹ The ring-opened EC is highly reactive and can undergo multiple chemical reaction steps leading to alkoxycarbonate ($\text{R}-\text{O}^{\cdot-}$) radicals. These radicals can subsequently lead to an autocatalytic EC ring-opening reaction forming PEG and CO_2 (reaction 4.3)



On the other hand, below **1.6 V** the evolution of H_2 gas is observed and likely due to the electrochemical reduction of H_2O , present in trace amounts as impurity (reaction 4.4)



The reduction process corresponding to the peak starting at roughly **1.0 V** is assigned to several processes involving CO_2 consumption (negative evolution rate of $\text{CO}_2 < 1 \text{ V}$, Figure 4.2 (b)) and H_2 evolution (reaction 4.5, 4.6, 4.7)



After monitoring the gaseous reaction products evolved during the negative polarisation of Au electrode with OEMS, the solid electrode deposits are explored with the help of SERS. For that SERS active Au electrode is polarised against Li in the model electrolyte and SERS spectra are recorded at definite potential interval.

4.1.4 *Operando* Raman spectroscopy

Figure 4.3 displays an overview of the *operando* Raman results for the SEI formation on the model Au electrode using LiClO_4 in EC electrolyte. Detailed Raman band assignment are presented in Figure 4.3(a) and can be found in table S1 of the **paper I**. Figure 4.3(c) presents the changes in intensities for the electrolyte induced Raman signals and the appearance of new signals as a function of applied potential.

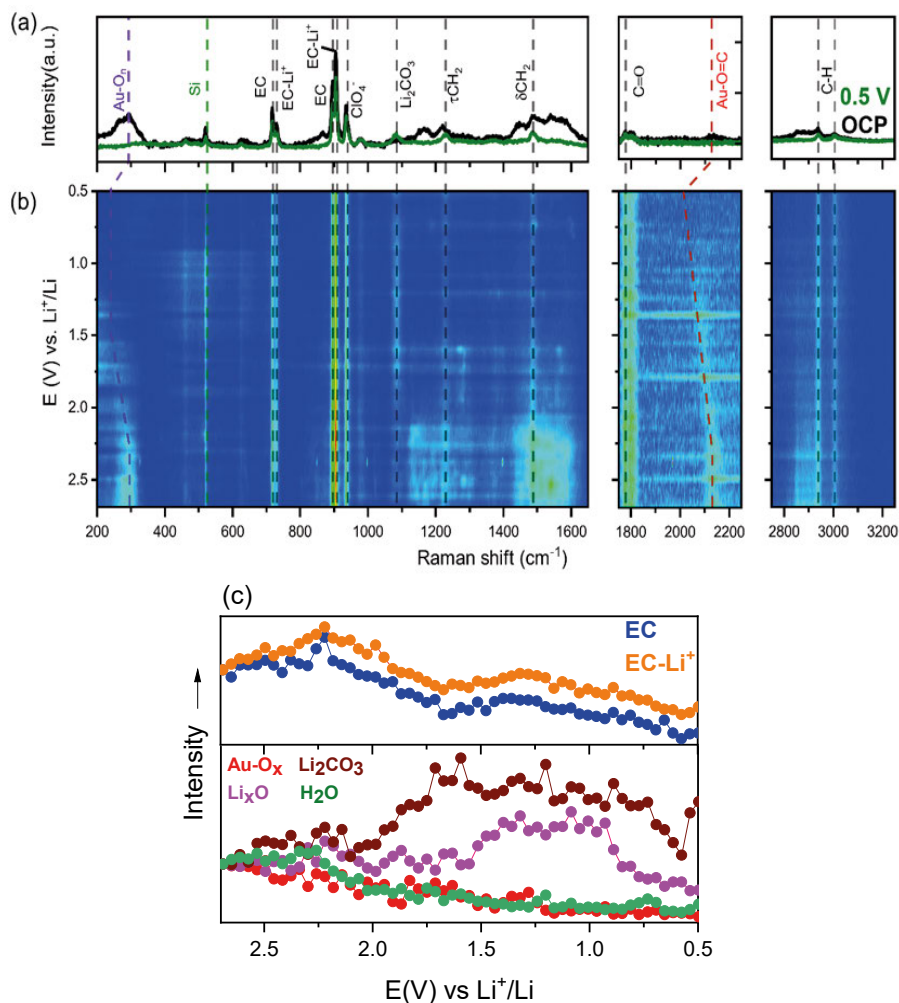


Figure 4.3: (a) Raman spectra recorded on Au SERS substrate used as working electrode in LiClO_4 :EC at OCP and 0.5 V against Li^+/Li . The assignments of the various peaks are presented with dashed lines, (b) Contour plot showing *operando* Raman spectra during the first reduction half cycle, (c) fitted intensities of the selected Raman peaks. Each fitted intensity is normalized against the intensity of the respective peak in the OCP spectrum. Reprinted with permission from reference.¹

The highest intensity peaks belong to the individual molecular species of the electrolyte, namely LiClO_4 and EC. In addition to that, impurities in the form of H_2O , carbon and oxygen containing species (hereafter denoted as $\text{O}=\text{CR}$ and $\text{O}-$, respectively) adsorbed on the Au substrate are detected in the Raman spectrum recorded at OCP, *i.e.*, before enforcing any external potential to the electrodes.

The respective signals for adsorbed $\text{O}=\text{CR}$ to uncoordinated Au site (marked by red vertical dashed line as $\text{Au}-\text{O}=\text{C}$) and adsorbed $\text{O}-$ containing species (marked by purple vertical dashed line as $\text{Au}-\text{O}_n$) are observed to undergo a shift as a function of applied potential from 2070 to 2133 cm^{-1} and 292 to 220 cm^{-1} , respectively. This is due to the Stark effect, and is indicative of chemisorbed species on the electrode surface.⁷⁰ Residual H_2O that is observed as a broad peak at $\sim 1617 \text{ cm}^{-1}$ is seen to fade away at the same time as when H_2 is observed to evolve in the OEMS experiment, and hence this is suggestive that H_2O undergoes electrochemical reduction that leads to the formation of H_2 .

The Raman peaks of EC solvated to Li^+ , hereafter denoted as $\text{EC}-\text{Li}^+$, (727 and 905 cm^{-1}) show significant increase in intensity with a maximum at 2.3 V. At potentials < 2 V, a synchronous drop in peak intensity for all vibration bands is observed and correlates with the onset in electrochemical reduction current (Figure 4.2). Increase in $\text{EC}-\text{Li}^+$ peak intensity upon negative electrode polarisation is assigned to the build-up of coordinated EC during charging of the EDL at the Au electrode surface. A minor increase is also observed in the intensity of the vibrational mode corresponding to free/uncoordinated EC at 717 and 894 cm^{-1} . This is in contrast to the observations made previously in our group⁵⁸ although for a more dilute Li-salt electrolyte, 1M LiPF_6 in EC:DEC (1:1 v/v). Thus, it can be inferred that the solvent-salt coordination structure is likely different in the higher salt concentrated electrolyte studied herein.

An emerging band at 1085 cm^{-1} corresponding to Li_2CO_3 is observed at < 2 V and partly associated with the two-electron EC reduction pathways also leading to the C_2H_4 evolution as can be seen in the OEMS measurement (Figure 4.2). The intensity of the band remains constant until 1.0 V where a small decrease is observed, but the band is still present until 0.5 V indicating that Li_2CO_3 stays on the electrode surface.

Another band at 523 cm^{-1} that can be associated with Li_xO is observed to grow slowly at < 2 V. It is expected to form as a result of reduction of surface contaminating Au-adsorbates (*e.g.*, $\text{Au}-\text{O}_n$ species) which when contact Li^+ , can deposit as SEI constituent. These lithium oxides, a type of LB, are known to be reactive towards both EC and CO_2 , leading to the formation of more thermodynamically stable products, such as Li_2CO_3 , on the Au surface.⁷¹ This is again in-line with the OEMS gas experiment, where, consumption of CO_2 and further evolution of H_2 was observed as the potential starting ~ 1.0 V.

As discussed earlier, impurities are notoriously difficult to get rid of. Generally, they make the dataset irreproducible and often misleading. Another realisation made in this study is that depending upon the proximity of the analyte species and SERS substrate and how they interact with each other, the surface enhancement of certain species is much favoured over others.

The conclusions drawn from the trends observed thus far are underpinned by and complement previous reports with much more details of the formation of the SEI. The findings provide a more complete overview on how the step-wise reduction of various electrolyte species (including impurities) and the intricate dynamics of Li^+ solvation/coordination are driven by potential. EC is found to be highly active and both reductively and chemically decompose to form Li_2CO_3 dominating the SEI. Environmental gases such as O_2 and CO_2 take active part in adsorption, diffusion and even surface electrochemistry.

4.1.5 Practical considerations and limitation

Reproducibility is a major challenge for our *operando* experiments. Small variations in the electrolyte (due to degradation over time, water adsorption, gas adsorption/desorption) contaminants from cell part affect the outcome of each measurement strongly.

Moreover, the lack of understanding of the mechanism of signal enhancement makes it challenging to optimize experimental conditions. For our measurements, it seems like the enhancement due to chemical enhancement of the target molecules (i.e., the nanometric SEI species) being able to transfer electrons to/from the metal particles is more pronounced than the electromagnetic enhancement (i.e., associated with plasmon excitation in SERS substrate). For example, due to the specific interaction of Li_2CO_3 with the SERS substrate, a specific vibrational mode of the molecule experiences a change in electron density. This induced change in electron density alters the molecular polarizability and, consequently, enhances the Raman signals associated with the specific vibrational mode of those molecules. For the exact determination of the enhancement mechanism, accurate atomistic *abinitio* calculations based on time-dependent DFT that considers the actual distribution and configuration of atoms within a gap could be performed.⁵⁴

4.2 Reaction mechanisms of electrolyte additives

4.2.1 VC

4.2.1.1 Electrochemical vs. chemical reactions of VC

- Electrochemical reactions

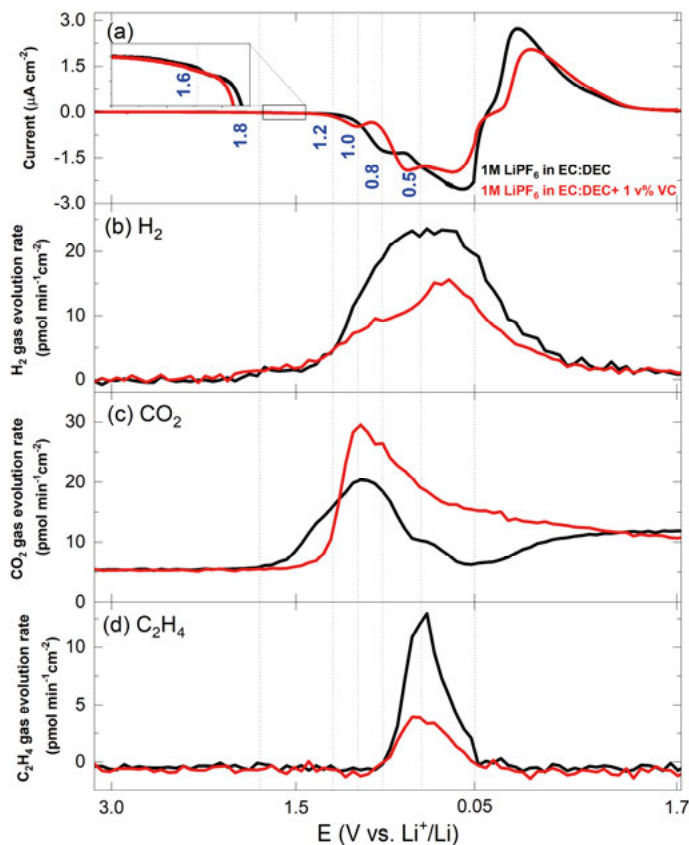
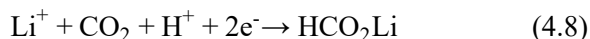


Figure 4.4: (a) Cyclic voltammogram from GC|LP40| LFP OEMS cell with (red) and without VC (black) cycled with CV at 0.1 mV/s rate, with a zoom-in on ~ 1.6 V electrochemical profiles. Simultaneous (b) H_2 , (c) CO_2 and (d) C_2H_4 gas evolution rates ($\text{pmol min}^{-1}\text{cm}^{-2}$) as measured.

Figure 4.4 displays the cyclic voltammogram alongside simultaneous profiles of H_2 , CO_2 and C_2H_4 gas evolution of GC|LP40| LFP OEMS cell containing 1M LiPF_6 in EC:DEC (1:1 v/v) with (red) and without 1 v% VC (black). Glassy carbon electrode was utilised as the negative electrode instead of typical graphite to observe (electro-)chemical surface reactions independently of solvent co-intercalation with Li^+ into graphite. The current is predominantly governed by de-/adsorption of Li^+ in the nanoscale surface crevices of glassy

carbon.⁷² In absence of VC, a minor current peak associated with H₂O reduction is observed <1.6 V vs. Li⁺/Li (see Figure 4.4 (a) inset), followed by EC and CO₂ reduction <1.0 V. Conversely, in the VC containing electrolyte, there is no clear indication of H₂O reduction observed in the current profile, although H₂ is evident in the OEMS gas data. *Operando* H₂ gas evolution rate also shows that the amount of H₂ evolved when VC is added is less. These observations point to the fact that VC interacts with water in the Li-ion cell. At ~1.2 V, a new current peak is observed when VC is present and likely related to Li-formate (HCO₂Li) formation (reaction 4.8)



This reaction involves proton consumption, explaining the lower H₂ evolution rate. Again <1.0V, direct CO₂ reduction initiates. The VC-derived SEI layer suppresses EC reduction, evidenced by the lower evolution of C₂H₄ and is more resistive as less reversible current is observed.⁶⁵ Although CO₂ generation commences later when VC is present, the CO₂ gas evolution rate rises steeply at 1.4 V and the amount of CO₂ evolved is higher than the blank cell. If we consider one mole of VC converts into one mole of CO₂, and that all the CO₂ observed for VC electrolyte is solely from VC decomposition, then only ~10 % of the added VC in the electrolyte would be used up. Moreover, the CO₂ evolution observed for VC which continues after the end of the reductive CV scan could belong to a chemical chain reaction which eliminates CO₂.²⁸

From this experiment, it is learned that both EC and VC are prone to ring-opening and CO₂ release, although the rate of the reactions are different. The presence of EC and VC together in the electrolyte however makes it difficult to decipher the VC-responsible reactions from those of EC. In order to understand the individual reduction reaction pathways, the electrolyte formulation was further simplified: DME was taken as a background and the electrochemical reactions in only VC containing cells were probed with the help of *operando* gas analysis and compared them with when EC is also added in the electrolyte mixture. The amounts of VC and EC were varied in the electrolyte formulations in an attempt to favour a certain kind of reaction over the other.

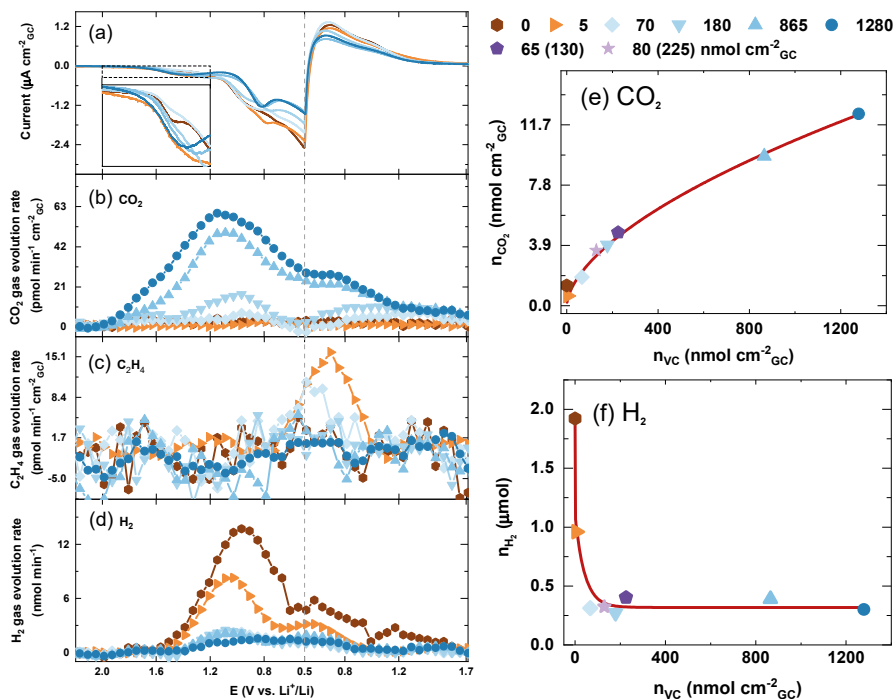


Figure 4.5: OEMS data for a GC| 0.2 M LiClO₄ DME:VC| LFP cell cycled with CV at 0.1 mV/s rate, (a) the electrochemical profile for the different cells during the initial cycle, with a zoom-in on >1.2 V electrochemical profiles (inset), electrolyte mixtures of increasing concentrations of VC (where n_{VC} is from 0 to 1280 nmol_{VC} cm⁻²_{GC}) (b) the CO₂ gas evolution trend in the initial cycle, (c) C₂H₄ gas evolution trend in the initial cycle, (d) the H₂ gas evolution trend in the initial cycle, (e) the total CO₂ evolution for different n_{VC} , (f) the total H₂ evolution for different n_{VC} . The cells denoted 65 (130) and 80 (225) are a mix of VC and EC (only shown in (e) and (f)), where the first value is n_{VC} and the value in parenthesis is n_{VC+EC} .

Figure 4.5 presents the (a) cyclic voltammogram and evolution profiles of (b) CO₂, (c) C₂H₄ and (d) H₂ for GC| 0.2 M LiClO₄ DME:VC| LFP cells with electrolyte mixtures of increasing concentrations of VC (where n_{VC} is from 0 to 1280 nmol_{VC} cm⁻²_{GC}). Figure 4.5 (e) and (f) shows the total CO₂ and H₂ evolved for all the cells with VC along with the cells containing both VC and EC (n_{EC} from 0 to 145 nmol_{EC} cm⁻²_{GC}). The cells denoted 65 (130) and 80 (225) are a mix of VC and EC (only shown in (e) and (f)), where the first value is n_{VC} and the value in parenthesis is n_{VC+EC} . The first observable electrochemical reaction occurs within the 1.9 – 1.6 V range as evident in the current profile (Figure 4.5 (a), see inset). All VC containing cells have a similar negative current slope down to ~1.4 V without a distinct H₂O reduction plateau compared to the pure DME baseline cell.

The two highest VC containing cells (≥ 865 nmol_{VC} cm⁻²_{GC}) reach a current peak at 1.4 – 1.3 V signifying the early formation of a fully-covering SEI layer.

This effect is less pronounced in cells with $\leq 180 \text{ nmol}_{\text{VC}} \text{ cm}_{\text{GC}}^{-2}$ cells, as seen in the inset of Figure 4.5 (a). A new current peak emerges $\sim 0.8 \text{ V}$ for the highest VC concentrations cells ($\geq 865 \text{ nmol}_{\text{VC}} \text{ cm}_{\text{GC}}^{-2}$) and coincides with CO_2 consumption $< 1.0 \text{ V}$.^{4,73} Comparable current intensity profiles are observed for cells with lower n_{VC} , albeit to a lesser degree.

CO_2 gas evolution is detected already $> 2.0 \text{ V}$ before the current onset at $\sim 1.9 \text{ V}$ for the cell with the highest VC concentration of $1280 \text{ nmol}_{\text{VC}} \text{ cm}_{\text{GC}}^{-2}$. This is early when compared to the experiment of VC added in LP40 mentioned previously, where CO_2 was observed $\sim 1.4 \text{ V}$ (Figure 4.4). A reason could be that there are other reactions suppressing CO_2 when LiPF_6 is present as salt. LiPF_6 likely dries the electrolyte as well, e.g., to form HF, which does not ring-open VC to the same extent.

CO_2 gas evolution is observed to shift to lower potentials and lower rates are detected with lower n_{VC} until no CO_2 is present in the baseline cell (Figure 4.5 (b)). CO_2 from VC at these potentials could stem from VC ring-opening induced by reduced surface oxygens, which are generated at potentials $< 2.6 \text{ V}$ vs. Li^+/Li ,⁴ as virtually no reduction current is detected at this stage. The CO_2 consumption reactions present $< 1.0 \text{ V}$ are linked to the simultaneous consumption of surface hydrogens. This is evident in the gas rate profile, where comparable indents appear in both CO_2 and H_2 gas evolution data (Figure 4.5 (b) and (d)), indicating the likely formation of HCO_2Li , as discussed earlier.

The OEMS data does not provide conclusive evidence on the extent of VC reaction. Nonetheless, given that the total CO_2 produced is significantly lower than the amount of VC initially present, it suggests the occurrence of reaction pathways where CO_2 is not released. This may involve the formation of various oligomers/polymers, maintaining the integrity of carbonate groups. This finding aligns with the results observed in the LP40 experiment with added VC (as discussed in Figure 4.4).

H_2 evolution onsets at $\sim 1.6 \text{ V}$ in all VC cells (Figure 4.5 (d)), but its rate is notably inhibited when a small amount of VC is present. Two distinct peaks in H_2 evolution are identifiable, with the second onset occurring at $\sim 0.7 \text{ V}$. The existence of these two peaks is likely linked to the formation of HCO_2Li at $\sim 1.0 \text{ V}$, leading to lowering in the rate of gas evolution. This suggests a primary H_2 -evolving process rather than two separate reactions, aligning with the findings of Metzger *et al.* where H_2 evolution was reported to mainly originate from H_2O reduction.⁷⁴ Importantly, irrespective of the quantity of VC, complete suppression of H_2 evolution never occurs. Instead, a plateau of $0.3 \mu\text{mol H}_2$ is reached at $70 \text{ nmol}_{\text{VC}} \text{ cm}_{\text{GC}}^{-2}$ and remains unaffected by higher n_{VC} . Therefore, there is likely another source of H_2 besides H_2O , with surface groups on the carbon serving as potential candidates.

Crucially, only cells containing VC evolves CO_2 (Figure 4.5(b)) compared to EC-only cells (figure S3 in **paper IV**), where CO_2 evolution remains below the detection limit. However, when mixing both VC and EC in the base DME

electrolyte an additional effect is observed (Figure 4.5(e)), as similar CO_2 levels are evident in $n_{\text{EC}+\text{VC}}$ cells compared to n_{VC} cells. This indicates that the VC reaction pathway releasing CO_2 does not differentiate between EC and VC during the propagation step, suggesting that ring-opened VC apparently can react with EC in the electrolyte. Importantly, the mixing of EC and VC does not alter the trend of H_2 gas evolution (Figure 4.5(f)), as the same plateau of $0.3 \mu\text{mol}$ is reached for the mixed EC+VC cells as for the VC-only cells. This demonstrates the independence of the CO_2 and H_2 evolving processes from each other.

- Chemical decomposition of VC

Thus far it can be concluded that VC is affected by water and in order to further elucidate possible hydro-chemical degradation process, an injection cell-coupled mass spectrometry was performed where VC was exposed directly to a LB, hydroxide in this case. Parallel experiments subjecting EC to the same conditions were performed for comparison.

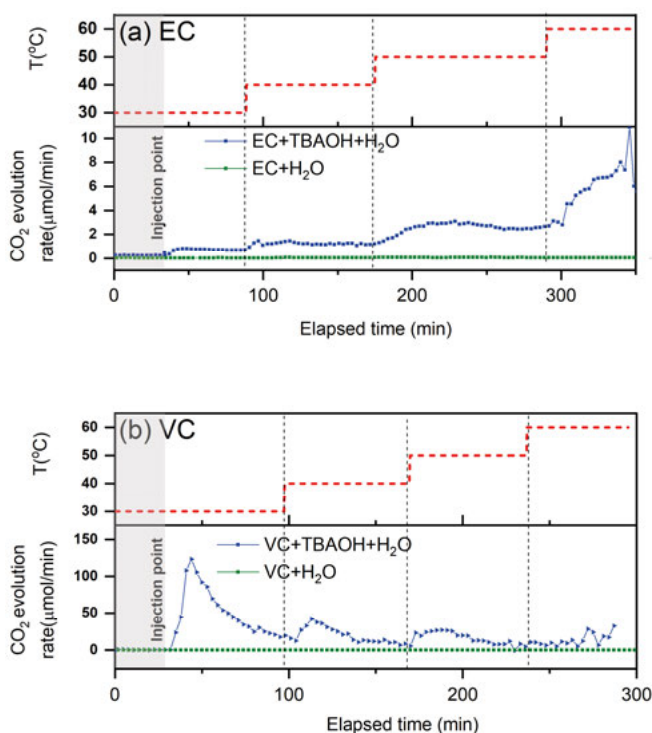


Figure 4.6: Red dashed line represents the temperature set point (upper panel) vs. time during (a) EC and (b) VC hydrochemical reaction, in presence (blue) and absence (green) of TBAOH in DME background solvent (lower panel). The evolution rate of CO_2 in the head space of the injection cell is represented in $\mu\text{mol}/\text{min}$.

Figure 4.6 shows CO₂ evolution over time when (a) EC and (b) VC are introduced into a solution of DME containing H₂O in absence (green) and presence (blue) of TBAOH. TBAOH is chosen over LiOH due to its higher solubility in DME, ensuring homogeneous reactions. DME, known for its superior chemical stability towards LBs, is selected to prevent interference from other carbonates and serve as a background solvent for comparing EC and VC ring-opening reactions under similar conditions.²⁰ The initial carbonate to OH⁻ ratio is 1:0.06 molar (and H₂O 0.18 mol). The upper panel in Figure 4.6 displays the temperature set point (red dotted line), with the grey area indicating baseline measurement time. The CO₂ evolution traces demonstrate the stark difference in reaction mechanism and kinetics for EC and VC hydrolysis in the presence of OH⁻ ions.

The apparent activation energy of EC hydrolysis driven by OH⁻ is determined to be ~64 KJ/mol from the Arrhenius plot, consistent with the findings of Metzger *et al.*⁷⁵ Compared to EC, hydrolysis of VC proceeds much faster and to a larger extent, making it challenging to estimate the activation energies. Despite this, the two-order-of-magnitude higher CO₂ evolution rate for VC suggests a substantially lower activation barrier for VC hydrolysis at room temperature than for EC. The released CO₂ interacts with nearby OH⁻ to form carbonates and bicarbonates (through reaction 4.9 and 4.10)



Once formed, these carbonates exhibit greater stability than OH⁻, thus preventing further OH⁻ reactions. In essence, CO₂ deactivates OH⁻, explaining the absence of an increased CO₂ evolution rate despite elevated temperatures. The slower CO₂ evolution rate for EC results in a prolonged deactivation of hydroxide, leading to temperature-dependent CO₂ growth. The localized high concentration of CO₂ appears to be a beneficial effect of VC.

The overall conversion of EC and VC was estimated by assessing the total evolved CO₂ at the end of each temperature step for all investigated electrolytes. Utilizing MS measurements, VC and EC consumption was calculated under the assumption that 1 mol of CO₂ originates from the decomposition of 1 mol of VC and EC, respectively (table I in paper II). Notably, there is no direct correlation between CO₂ evolution and the initial concentration of VC in the electrolyte, as a significant amount of unreacted VC and TBAOH.30H₂O molecules remains in the solution. This observation aligns with our OEMS experiment mentioned above (Figure 4.4), where ~90% of VC is found to remain unreacted.

Over time, the VC hydrolyzed solution exhibited degradation, evident through a progressively darker color and the eventual formation of an insoluble

ble, dark, gel-like precipitate at the vial's bottom. In contrast, the EC hydrolyzed solution remained colorless without any precipitation. NMR analysis was conducted on the gel-like product to identify solubilized reaction products, and the findings will be discussed later.

4.2.1.2 Kinetics of VC hydrolysis

Operando H_2 gas evolution rate during reductive sweep as represented in Figure 4.4 shows that less H_2 was evolved when VC was present in the electrolyte. H_2 is generally evolved from the reduction of trace water present in the cell. The reduced H_2 evolution could be attributed to two possibilities: firstly, the SEI formed due to VC reduction completely passivates the carbon surface, preventing H_2O reduction and subsequent H_2 evolution, or second possibility, where VC itself or some VC reaction product scavenges H_2O .

Thus, in order to test the hypothesis that VC is responsible for water scavenging, KFT was employed to quantify the amount of water being consumed.

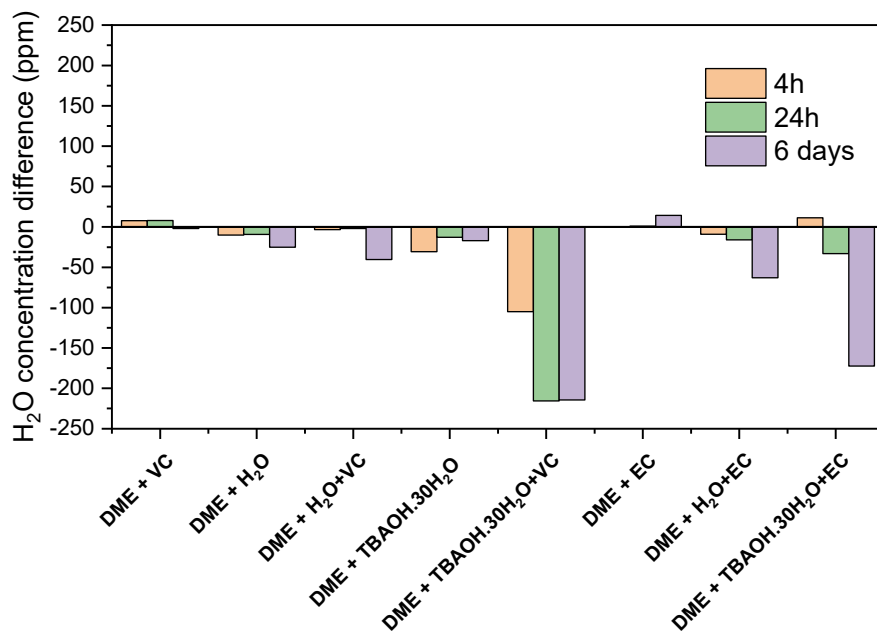


Figure 4.7: Amount of water consumed by VC and EC in presence and absence of OH^- at different reaction times. The amount of water present in the background solvent were also measured over the same period of time: 4 hours, 24 hour and 6 days after mixing and subtracted H_2O recorded at the time of mixing from them. The bar going down represents the consumption of H_2O .

KFT was conducted on a range of electrolytes deliberately contaminated with 667 ppm H_2O , both with and without TBAOH, featuring VC. A parallel ex-

periment was performed with a series of EC-containing samples for comparison. In Figure 4.7, the summary illustrates the water consumption in different electrolyte formulations and their respective blank standards, with the downward bars indicating H₂O consumption.

The findings reveal that in solutions with VC, the H₂O content remains stable for the initial 24 hours. A marginal decrease is observed only after storage exceeding 6 days. However, in the presence of OH⁻, VC exhibits a significantly accelerated rate of H₂O scavenging. Approximately 100 ppm of water is consumed within 4 hours and more than 200 ppm after 24 hours of storage. Intriguingly, the water content stabilizes with prolonged storage. EC exhibits a trend similar to VC but to a lesser extent. A substantial reduction in water content is only observed after 6 days of storage for DME+TBAOH.30H₂O+EC. This suggests that once a VC molecule undergoes reaction facilitated by hydroxide, it becomes adept at scavenging water. VC also autonomously consumes H₂O, albeit at a slower rate compared to the presence of hydroxide. This underscores the pivotal role played by ring-opened VC as an initiator of the water consumption process.

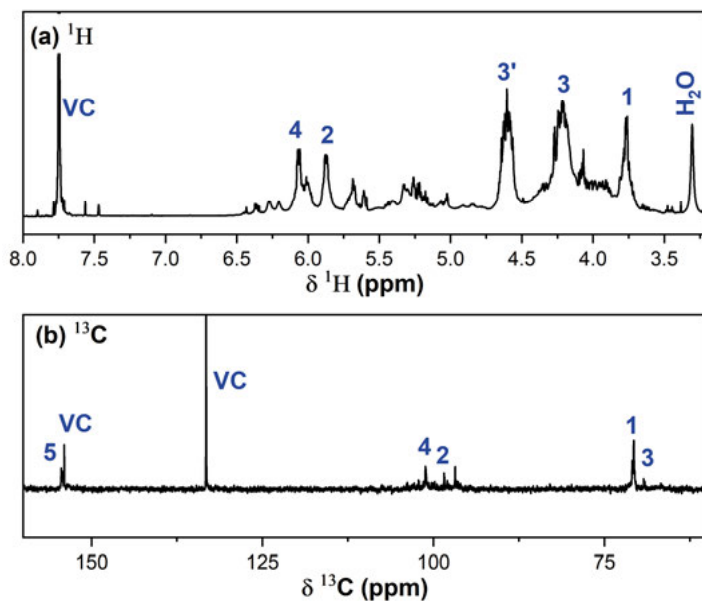
1.2.1.1. Identification of VC decomposition products

- Chemical decomposition products of VC

The solubilised reaction products were analysed with NMR spectroscopy. For that, the gel-like product was recovered from the injection experiment and then dissolved in DMSO-d₆. The residual DME solvent cast strong signals in ¹H NMR spectrum overlapping with most of the signals from the decomposition reaction product making the identification of the products extremely challenging. To address this, DME was substituted with DMSO-d₆, which not only eliminated signal interference but also offered improved solubility for the reaction products. A mixture of VC and TBAOH.30H₂O, in the same proportion as used in the injection experiment, was prepared. Figure 4.8(a) and (b) present the ¹H and ¹³C spectra for this mixture. The ¹H NMR spectrum (figure 4.8 (a)) shows a singlet at 7.78 ppm for the protons in the VC. The carbon peaks for -CH=CH- and C=O in ¹³C NMR spectrum (Figure 4.8(b)) for VC is at 133.2 and 154 ppm respectively. It is clearly observed that the spectra for the reaction product contain several new and weaker signals in both ¹H and ¹³C spectra, suggesting for a broader spread of hydrolyzed VC fragments. The NMR signal assignments were determined through a combination of complementary and detailed two-dimensional NMR experiments (¹H-¹³C HMBC and HSQC in Figure 4.8(c) and (d)). The HSQC experiment is used to determine proton-carbon single bond correlations, with the protons represented along the observed X-axis and the carbons are along the Y-axis. The HMBC experiment gives correlations between carbons and protons that are separated by two,

three, and, occasionally four bonds in conjugated systems. Within HMBC experiment, direct one-bond correlations are suppressed.

Two primary species have been identified with the NMR analysis and their structures are depicted in Scheme 4.1 as structure 1 and 2. Possible reaction schemes to form these species are proposed on the basis of the experimental data and are outlined in Scheme 4.1.



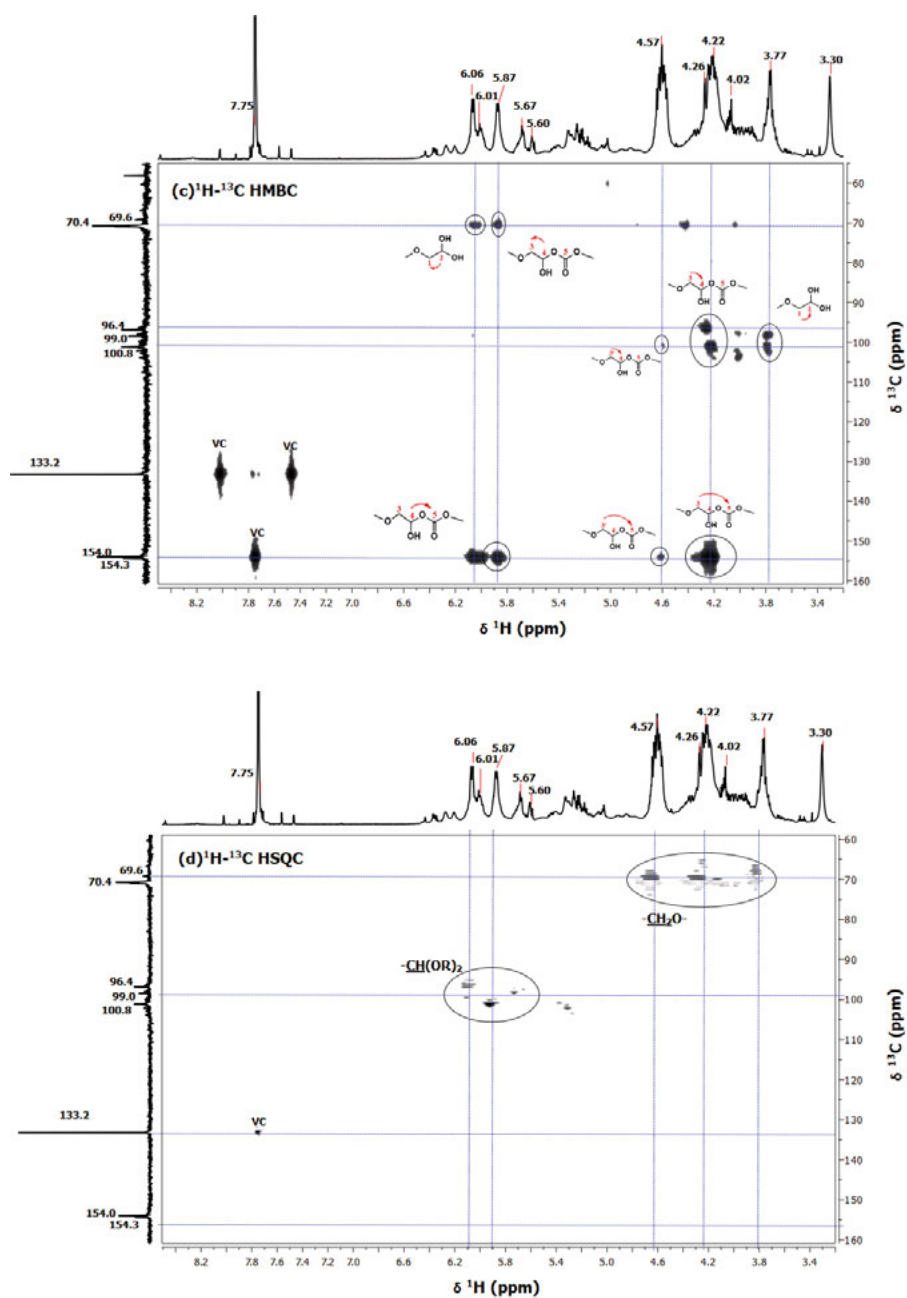
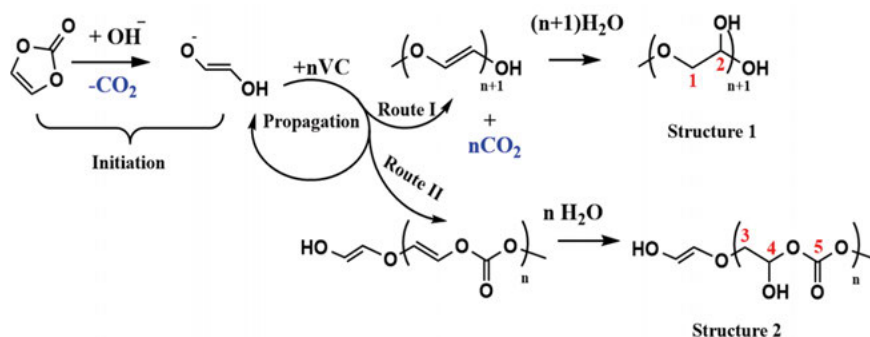


Figure 4.8: (a)-(d) ^1H , ^{13}C , 2D ^1H - ^{13}C HMBC and ^1H - ^{13}C HSQC NMR spectra of the solubilized VC reaction product. The numbers in blue in (a) and (b) are denoted to the carbons and protons that will be used for their assignment in table 2.



Scheme 4.1: Proposed scheme for chemical decomposition of VC. The numbers in red in the structures are denoted to the carbons that will be used for their assignment in table 2.

Structure 1: Based on the HSQC spectrum in Figure 4.8(d), the protons H1 at 3.77 and H2 at 6.06 ppm are seen to be directly attached to the carbon C1 at 70.4 ppm and C2 at 98.2 ppm respectively. In HMBC spectrum in Figure 4.8(c), protons H1 and H2 are seen to give a cross peak to C2 and C1, respectively. The carbon C2 at 98.2 ppm is assigned the O-C-O unit based on the chemical shift of the carbon. Based on this chemical shift, these signals fit to structure 1 as shown in Scheme 4.1.

The first step to form this product is the nucleophilic attack of the OH⁻ on the VC, leading to ring-opening of VC and CO₂ release. This process yields a vinylene glycol (-O-CH=CH-OH) moiety. Subsequently, this moiety can induce polymerization with additional VC molecules, forming longer chains that can undergo further CO₂ elimination, as shown as in *route 1* in Scheme 4.1. There is no direct evidence of vinylene glycol in the NMR analysis of this study. However, the formation of -CH(OR)₂ fragments in the product may plausibly occur when the double bonds of vinylene glycol undergo hydrolysis via a simple addition reaction, ultimately leading to a species with Structure 1. This proposed chemical reaction offers a plausible explanation for the observed water consumption during the chemical reaction.

Structure 2: Based on the HSQC spectrum in Figure 4.8(d), the protons H3 at 4.57 and 4.22 ppm are found to be directly attached to the carbon C3 at 69.6 ppm. As can be seen in the HMBC spectrum in Figure 4.8(c), the protons H3/H3' have a multi-bond correlation to the carbon C4 at 100.8 and carbonate carbon C5 at 154.3 ppm. Likewise, the protons H4 at 5.87 ppm have multi-bond correlation to the carbons C3 at 69.6 and carbonate carbon C5 at 154.3. Based on the HSQC spectrum, the proton H4 at 5.87 ppm and H3 at 4.57/4.22 were directly attached to the carbon C4 at 100.8 and C3 at 69.6 ppm, respectively. Based on this chemical shift, specie with structure 2 has been determined as shown in Scheme 4.1. These chemical shifts are in close agreement

with the NMR study made by Ota *et al.*, where they identified this compound as an SEI compound derived from VC.²⁴ The structure 2 is estimated to be a polymer component because the protons H3 and H4 consist of broad peaks. This is largely due to poor molecular rotation and repeating units being situated in marginally different chemical environments resulting into broad signals.

The structure 2 can plausibly form through a route (*route 2*) where the vinylene glycol moiety undergo polymerization reaction with other VC molecules without the evolution of CO₂. This reaction results in formation of polycarbonates. The double bond can again undergo simple addition reaction leading to the structure 2. There is also possibility that these two polymer chains, with structures 1 and 2 as the repeating units, could be part of the same polymer chain.

Although the proposed reaction pathway for generating these chemical species seems plausible, it is not conclusive, allowing for the potential formation of additional species that could produce similar chemical signatures.

Table 2. ¹H and ¹³C NMR chemical shifts of the soluble products formed from VC decomposition

¹ H chem. shift (ppm)	¹³ C chem. shift (ppm)	Assignment	Molecular Fragments	Corresponding structure
3.77	70.4	1	-CH ₂ O-	Structure 1
6.06	98.2	2	-CH(OR) ₂ -	
4.57, 4.22	69.6	3	-CH ₂ O-	Structure 2
5.87	100.8	4	-CH(OR) ₂ -	
-	154.3	5	-O(C=O)O-	

Additionally, there is no evidence of poly(VC) which implies that poly(VC) must be a product of electrochemical reduction of VC and not a product of VC chemical decomposition. However, it could also be that poly(VC) is insoluble, hence not detected with solution NMR.

- Electrochemical decomposition product of VC

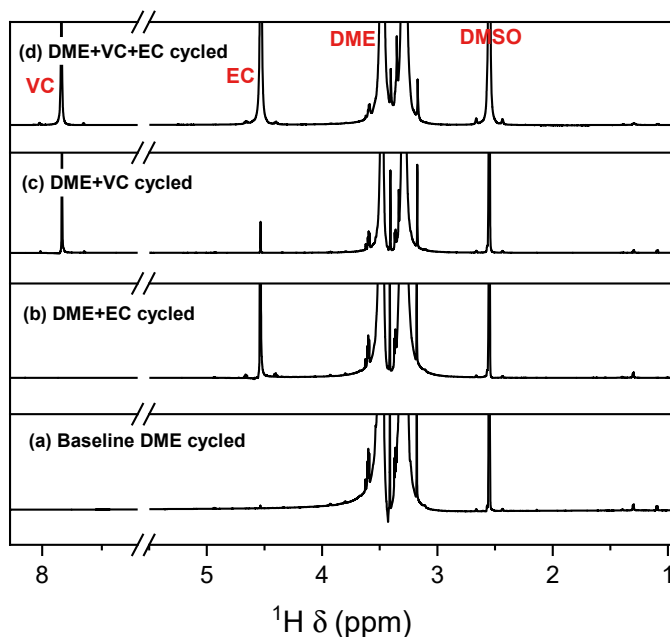


Figure 4.9: ^1H NMR spectra of electrolyte extracted from GC | 0.2 M LiClO_4 DME + VC + EC (0 or 10 v%, respectively) | LFP cells cycled at constant current until 0.5 V and held at the potential for 3 h.

The electrolytes from the cycled OEMS cells were extracted and analyzed with NMR spectroscopy in an attempt to detect electrochemically decomposed products of EC and VC that remain solubilized in the DME electrolyte. The ^1H NMR spectra are presented in Figure 4.9. No clear evidence of soluble reduction products was detected in either EC or EC:VC cells. However, the VC containing cell clearly shows an extra peak in ^1H NMR after cycling, and this signal coincides with EC. A similar effect was detected with OEMS (Figure 4.5 (c)), where C_2H_4 was detected in cells at low n_{VC} even though no EC ($n_{\text{EC}} = 0$) was added. It is therefore proposed that VC can abstract reduced protons from the GC surface and turn into EC. The reason for only detecting C_2H_4 at low n_{VC} in the OEMS is due to the VC-derived SEI not fully covering the GC surface and the EC thus formed can be reduced at the uncovered GC surface to the extent it is detectable.

Additionally, another NMR series was investigated, where the DME electrolyte was exchanged for DMSO-d_6 in an attempt to identify possible SEI products (as presented in SI of **paper III**). Lithium formate was detected, which agrees with the OEMS conclusions. Additionally, vinoxyl groups ($\text{CH(=O)-CH}_2\text{R}$) as well as a range of VC-derived polymeric fragments are present. Notably, PEG forms in the EC-only cell, but is completely suppressed

if also VC is included, hence demonstrating that VC suppresses EC hydrolysis and the subsequent formation of PEG. Additionally, there is no evidence of poly(VC) in cycled electrolyte with VC. This could mean that poly(VC) is a solid, hence not detected with solution NMR.

These findings contribute to a more profound comprehension of the diverse chemical and electrochemical reaction pathways of VC. Distinct behaviors of EC and VC are observed both in isolation and when combined. Essentially, both carbonates undergo ring-opening processes, with the VC process occurring more rapidly and extensively. Once VC is ring-opened, it efficiently scavenges traces of water from the cell.

4.2.2 TMSPa

4.2.2.1 Mechanisms involving TMSPa and Lewis bases

SEI dissolution and reactivity towards other cell constituents (*e.g.*, solvents) during the course of cell cycling is a major concern for the capacity retention, cell lifetime and safety. The SEI is mostly composed of LBs, out of which F^- , OH^- , and OCH_3^- being notable ones. F^- is formed as a result of decomposition of fluorinated salts and additives like FEC. LiF is practically insoluble in the solvents and hence precipitates on the electrode surfaces whenever formed. OH^- is typically formed from the reduction of trace water in the electrolyte.⁷⁷ OH^- may also result from the reaction of Li_2O with water.⁷⁸ LiOH is predicted to be more soluble than LiF in conventionally used solvents.⁷⁹ OCH_3^- may form as a result of electrochemical reduction of semicarbonates like DEC. The solubility of $LiOCH_3$ is predicted to lie in between LiF and LiOH.⁷⁹

In this chapter, the reactivity of these LBs (F^- , OH^- , and OCH_3^-) in EC:DEC (1:1 v/v) based solvents is investigated with the help of TMSPa, where the additive molecule acts as a chemical probe and scavenger. For that lithiated LBs are mixed in EC:DEC solvents, with and without the additive, and the reaction products are monitored. 1H , ^{31}P and ^{19}F NMR combined with headspace gas analysis are employed to track the TMSPa, LBs, solvents, as well as both soluble and volatile reaction products. The anticipated reaction products were confirmed by referencing the pure compounds.

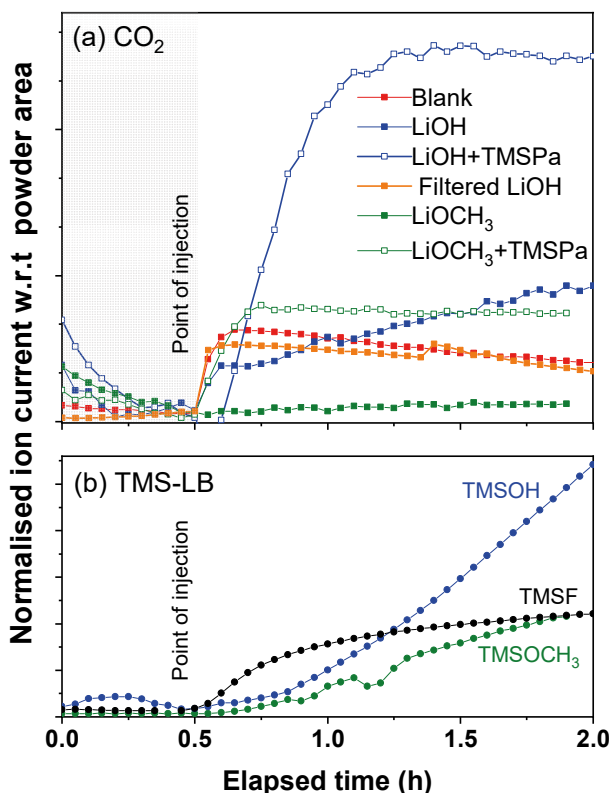
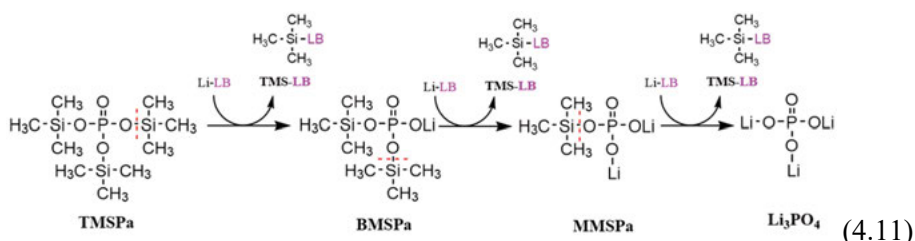


Figure 4.10: (a) CO₂ gas evolution profile of blank solution and LBs with solvents with and without TMSPa. Grey area represents the region of background baseline. (b) TMS-LB evolution profiles, as recorded from the mass spectrometer. Reprinted with permission from reference.²

First, the NMR spectroscopy and gas evolution were performed to investigate the blank experiment, *i.e.*, for the solution mixture containing only EC and DEC (without any LB). NMR indicated the presence of trace H₂O in the solution mixture, while MS showed the release of already dissolved CO₂ gas from the solvents that escapes due to the continuously flushed Ar headspace (shown by the gas profile in Figure 4.10 (a)). A small amount of CO₂ gas is often present in the solvents that is formed as a result of solvent degradation over time just by sitting idle inside the glove box. This experimental finding is an indication of the sensitivity of the instruments used in this study and is used as reference for the forthcoming experiments as lithiated LB and TMSPa are introduced into the system.

Upon monitoring the reaction product of a solution based on LiOH mixed with EC:DEC solvents, it was found out that OH⁻ causes EC polymerisation resulting CO₂ and EG moieties (reaction 1.16). Evolution of CO₂ was observed in MS experiment (Figure 4.10 (a)) and formation of solubilised EG was detected in NMR spectrum (Figure 1 in **paper IV**). Upon introducing

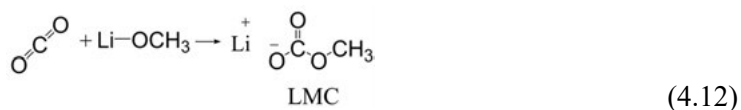
5v% TMSPa in the LiOH/EC:DEC mixture solution, evolution of CO₂ significantly increases. TMSPa is believed to act as ‘anion receptor’ enhancing the solubility of OH⁻ in the solvents. Higher concentrations of OH⁻ leads to the formation of much more PEG (according to the reaction 1.21), other solvent degradation products, and trimethylsilanol (TMSOH). TMSOH, in the gas form, is identified under MS (Figure 4.10 (b)). In addition to that, a small amount of TMSOH is solubilised in the solvents, hence detected with NMR (Figure 1 in **paper IV**). The TMS-units attached to the central phosphate group of TMSPa is expected to be consumed in a stepwise manner until only the final product, Li₃PO₄, without any TMS units attached remains (reaction 4.11).



The low solubility and low vapor pressure of the Li₃PO₄ makes it impossible to detect with the methodologies used in this study.

The intermediate compounds bis-(trimethylsilyl)phosphate (BMSPa, loss of 1 TMS unit from TMSPa) and mono-(trimethylsilyl)phosphate (MMSPa, loss of 2 TMS units from TMSPa) are detected with ³¹P-NMR and ¹H-NMR spectroscopy. This result is indeed supported by computational calculations (GFN2-xTB⁸⁰ and DFT).² In addition to that, TMSPa is observed to scavenge H₂O, present as trace impurity, resulting into TMSOH and BMSPa. Thus, in a practical perspective, TMSPa is desired in commercial cells.

Extending the study to OCH₃⁻, another commonly found LB, and looking at the gas evolution upon mixing the LB with the solvents, it was found that OCH₃⁻ scavenges CO₂ (Figure 4.10(a)) forming lithium methyl carbonate (LMC) following the reaction 4.12



LMC is often a well-reported SEI component with poor Li⁺ conductivity^{81,82} and is detected with NMR in this study. On introducing TMSPa into the system, the additive molecule is found to be completely consumed resulting in BMSPa and TMSOCH₃ as was seen in the ¹H and ³¹P NMR spectra. Additionally, TMSOCH₃ was clearly detected by the MS when TMSPa comes in contact with LiOCH₃ (Figure 4.10 (b)). Indeed, computational calculations for

TMSPa/LiOCH₃ reaction shows that the formation of MMSPa is energetically unfavourable, thus stopping the reaction at the most likely reaction product, BMSPa, and not proceed further to MMSPa or Li₃PO₄.

LiF, on the other hand is found to not react with the solvents. This is simply because of the very low solubility of these fluorides in the EC:DEC solvents. When TMSPa was added to the LiF in EC:DEC mixture, TMSF is evolved as seen in ¹H and ¹⁹F NMR as well as in the headspace gas analysis experiment (Figure 4.10(b)), thus confirming that the reaction pathway follows reaction 4.11.

In conclusion, this study highlights that LBs take part in a series of competing thermally activated processes complicating the whole SEI formation process. Combining solution NMR and *in-situ* gas evolution experiments help us to analyse the reactions qualitatively. On the basis of the findings, it can be said that TMSPa is able to scavenge a number of potentially harmful LBs generated in the cell during cell operation. TMSPa derives its reactivity from its silyl functional groups. OH⁻ leads to EC ring-opening reaction forming resistive deposits of glycols/oxides and release of CO₂. Methoxide often reacts with CO₂ to form resistive LMC in the cell. Additionally, LiF is known as a resistive SEI specie. Therefore, introducing silyl functionalised electrolyte additives, such as TMSPa, in battery electrolyte could help us to scavenge harmful LBs and eventually replace them with the more ionically conducting Li₃PO₄.⁸³ These findings therefore explain why Li-ion cells with silyl-group-based additives display lower impedance and longer cycle life.

4.2.2.2 Reactivity of TMSPa and H₂O

It was found from this earlier study that the molecular mechanism behind the scavenging of LBs relies primarily on the Si-O bond of the TMSPa undergoing cleavage while the reaction with the LBs forming presumably less harmful organosilicon residues (TMS-LB) as products. Although it was found out experimentally that TMSPa scavenges H₂O in an environment of EC:DEC forming TMSOH and calculations of the first step of TMSPa/H₂O reaction showed that the hydrolysis of TMSPa is slightly exothermic, the later steps in the H₂O and TMSPa reaction mechanism were not clarified. H₂O is an unavoidable impurity present in organic electrolytes and well known to detrimentally affect all components of the battery. Despite numerous reports on the observation of Si-O bond cleavage and the formation of different silane-derived species in batteries containing TMSPa, a complete understanding of the underlying reaction pathways is lacking. This results section addresses to clarify the fate of the resulting silane products.

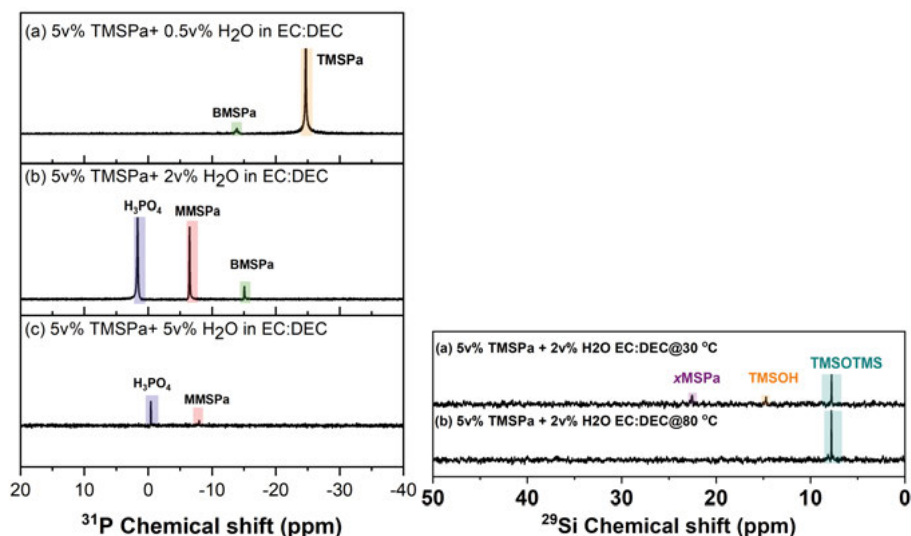
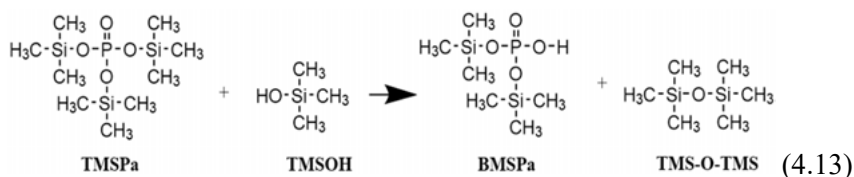


Figure 4.11: on left, ³¹P NMR of 5 v % TMSPa added in EC:DEC that is contaminated with (a) 0.5, (b) 2, and (c) 5 v % H₂O in the EC:DEC, on right, ²⁹Si NMR of 5 v % TMSPa in EC/DEC with 2 v % H₂O shows the presence of TMSOTMS. Reprinted with permission from reference.³

EC:DEC (1:1 v/v) was now deliberately contaminated with different amounts of H₂O (0.5, 2, 5 v%). 5v% TMSPa was then added to the freshly made contaminated solution. ³¹P NMR spectra for TMSPa and H₂O mixtures in the EC:DEC confirms further that TMSOH, phosphoric acid and its derivatives are formed upon reaction between TMSPa and H₂O (as can be seen in Figure 4.11(a)). It was also found out that increasing the amount of H₂O, while keeping the amount of TMSPa constant in the reaction mixture (5 vol % TMSPa in EC:DEC contaminated with 5 vol % H₂O), forces the equilibrium of reaction 4.11) to further right, favoring the formation of TMSPa molecule, which has lost at least one of its TMS units and hence TMSOH. On the other hand, lowering the amount of H₂O in the mixture (5 vol % TMSPa in EC/DEC contaminated with 0.5 vol % H₂O) shows that the reaction stops at BMSPa, while most of TMSPa remains unreacted in the solution.

A dimer of TMSO- group (namely, TMSOTMS) was also detected in the TMSPa and H₂O mixtures in the EC:DEC with the help of ²⁹Si NMR. It was found out to form as a result of side-reaction between TMSOH with the parent TMSPa molecule (through reaction 4.13)



Upon ramping up to higher temperature, the signals for TMSOH and TMSPa disappear whereas TMSOTMS grows. This indicates that the reaction of TMSOH with TMSPa forming TMSOTMS is as expected further enhanced at elevated temperature. The formation of TMSOTMS has been previously reported in papers where TMSPi was used as electrolyte additives.^{84–87} Most of these studies credit F[−] scavenging effect of TMSPi for the TMSOTMS formation, although the exact chemical reaction pathway leading to this TMSOTMS was not discerned.

Thus, it is concluded that the breakage of O-Si enables the formation of TMSOTMS, which then might remain as non-reactive specie in lithium-ion cell.

- Implication of decomposition products and mechanism

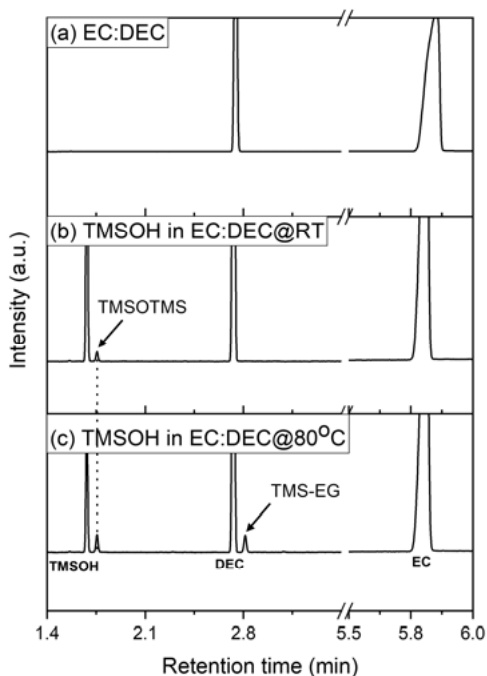
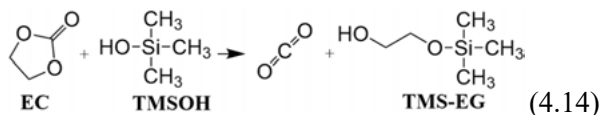


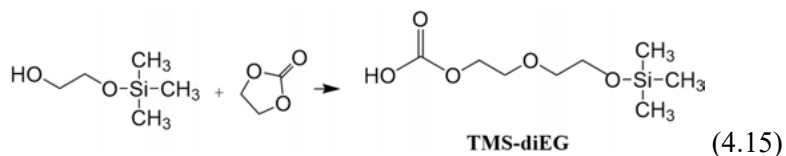
Figure 4.12: GCMS chromatogram of (a) EC:DEC baseline, (b) 5 v % TMSOH in EC:DEC at RT, and (c) 5v% TMSOH in EC:DEC at 80°C. EC and DEC appear at 5.79 min and 2.74 min respectively. TMSOH is observed as a signal at the retention time of 1.68 min. Reprinted with permission from reference.³

Having established that TMSOH is a rather reactive intermediate during hydrolysis of TMSPa, an alternative fate of the compound is further elucidated, which potentially affects practical cell performance. For that purpose, 5v% TMSOH was introduced in EC:DEC and then analysed using GCMS. The GCMS chromatogram of the mixtures are presented in Figure 4.12. The chromatogram recorded at RT reveals that TMSOH is not involved in any recordable side reactions with the carbonate solvents. The chromatogram of the mixture still shows the existence of TMSOTMS which is the by-product remains from the TMSOH synthesis process. This result is further complemented by NMR spectroscopy.

Upon increasing the temperature, TMSOTMS was found to still remain, however the signal for TMSOH decreases and a new signal appears at retention time of 2.87 min. This signal is attributed to a TMS derivative with ethylene glycol (hereafter denoted as TMS-EG), formed as a result of a ring-opening reaction of the surrounding EC molecule triggered by TMSOH (reaction 4.14)



This reaction also leads to the formation of carbon-dioxide. There is also possibility that TMS-EG further induces reaction on the surrounding EC solvent molecule forming longer polymeric chains of TMS-EG, denoted as TMS derivative with diethylene glycol (TMS-diEG) (reaction 4.15)



Evidence of this TMS-diEG was found in ^{29}Si NMR spectra presented in figure 5 (c) in **paper V**.

Thus, to conclude, Si–O bonds within TMSPa react with residual H_2O in the presence of carbonate solvents to form TMSOH and H_3PO_4 . TMSOH reacts subsequently with unreacted TMSPa to form the less reactive TMSOTMS dimer. A risk, however, is that the resulting TMSOH provides a nucleophilic attack on and ring-opens EC to form TMS-EG, albeit at a very low rate at RT. The activation energy required to open up EC ring by TMSOH is much higher than the energy required by the significantly more mobile H_2O . In a practical scenario it is highly desirable to let TMSPa scavenge H_2O to form less reactive TMS-based compounds. This also hints in the direction that H_2O is a stronger nucleophile than TMSOH. The computational results further suggest that the

ability of the reaction products to form energetically favourable intermolecular interactions such as hydrogen bonding is important for an efficient breakage of the O–Si bond of TMSPa.

5 Conclusion and future outlook

A chemically stable, Li^+ conducting, thin and passivating solid electrolyte interphase on the negative electrode surface is generally acknowledged as a prerequisite for a well-functioning lithium-ion cell. However, there is no real consensus regarding the SEI formation mechanism and the resulting structures in the research community. In literature, models ranging from single- to multi-layer, up to hetero-phase structures have been presented, but validation experiments are challenging and data interpretation is difficult and ambiguous.

In this thesis, a model spectro-electrochemical system is applied to simplify and study the complex SEI formation mechanism in Li-ion cell. In order to isolate the products of ethylene carbonate reduction, electrolyte based on LiClO_4 in EC and Au as the model working electrode are used. *Operando* surface enhanced Raman spectroscopy complemented by online-electrochemical mass spectrometry provides insights regarding the step-wise electrochemical reduction of electrolyte constituents during SEI formation. Various electrochemical surface processes, such as solvent reduction, are found to be functions of applied potential and electrode/electrolyte impurities play a significant role in the SEI build-up. Residual water as well as carbon and oxygen containing impurities (such as O_2 and CO_2) are found to interfere with the SEI formation mechanism. Regardless of electrolyte composition, lithium carbonate and lithium oxide are the dominating SEI species revealed by SERS, which forms already at ~ 2 V vs. Li^+/Li . Effects associated with electric double layer charging, electrode adsorbate polarization (Stark effect), and SEI dissolution are recognised. Although SERS provides deeper insights into the underlying mechanisms, it comes with a few limitations such as the technique is the most effective only when the analyte molecule interacts strongly with the substrate.

Electrolyte additives are functional molecular compounds included in low concentrations in Li-ion cells to enhance performance. The most common additive in modern Li-ion cells is VC. VC is an SEI former, which is decomposed before the electrolyte above 1 V vs. Li^+/Li and shown to suppress EC decomposition. VC has been not only known to polymerize, forming poly(vinylene carbonate), but also to release major amounts of CO_2 , which are two seemingly contradictory processes. So, the formation mechanism of CO_2 from VC decomposition in electrolyte is thoroughly studied herein, in an attempt to understand its implication on the SEI formation processes. It is found that a

huge amount of CO_2 is generated when VC is present as an electrolyte additive. This is because the activation energy of decomposition of VC to produce CO_2 is lower than its saturated counterpart, EC. The first step in VC degradation is the ring-opening which is rather a chemically activated process, for example, a hydro-chemical reaction of VC. This also produces a mixture of different solubilized polymeric/oligomeric chain fragments as detected by solution NMR.

During SEI formation, the CO_2 that is formed from VC degradation is subsequently reduced forming formate that eventually can contribute to the SEI. VC is also seen to lower H_2 evolution in the cell. This is credited to the ring-opening processes of VC that subsequently consumes H_2O . This hypothesis was proven by Karl-Fischer titration performed on a background solvent that was deliberately contaminated with water onto which VC was added with and without hydroxide. Moreover, it has also been shown in this thesis that VC can abstract reduced protons from the negative electrode surface and turns into EC.

Li-ion cells are assembled in dry room, so there is always some trace amount of water present. During initial polarization, water can reduce and form hydroxide on the negative electrode side. OH^- is likely the most potent of all Lewis bases (LBs) to trigger decomposition reactions *e.g.*, by autocatalytic decomposition of EC. Depending upon the solubility of the decomposed electrolyte specie, they can precipitate on the electrode surface leading to a thick SEI layer. Thus, an important functionality of VC is that it leads to a thinner SEI by cleaning up H_2O and hence suppressing H_2O reduction related processes.

In the later part of the thesis, the reactivity of LBs, commonly found in the SEI, towards electrolyte solvents is investigated. Tris(trimethylsilyl)-phosphate (TMSPa), a well-known representative of organosilicon-based electrolyte additives, has been used to chemically probe their reactivity and the underlying reaction mechanism involved. The reason for choosing TMSPa is that there are theories around it that it acts as multifunctional molecules: fluoride scavenger and CEI former in LIB cells. By combining *in-situ* headspace gas analysis and conventional solution nuclear magnetic resonance spectroscopy to qualitatively analyse the reaction products, it is concluded that the LBs are potentially harmful cell components as they lead to electrolyte degradation in the cell. Including TMSPa in small concentrations is effective in scavenging these LBs while replacing them with less harmful and electrolyte soluble trimethylsilyl-based components. The additive derives its main functionality from its silicon-oxygen bond. Intermolecular physico-chemical effects, such as anion reception is likely to be very important but remain a subject of future studies.

The follow-up study emphasized the reactivity of TMSPa with water in conventional organic carbonate solvents. Trimethylsilanol and phosphoric

acid are found as the main reaction products, however, various P–O–Si-containing intermediates are also found. TMSOH, a LB by itself, can as similar to water undergo reaction with TMSPa at room temperature to form hexamethyldisiloxane and as well as can also activate EC ring-opening reactions at elevated temperatures (≥ 80 °C) yielding a TMS derivative with ethylene glycol. While the formation of TMS-EG at the expense of EC is in principle an unwanted parasitic reaction, it should be noted that this reaction is only activated at elevated temperatures in comparison to EC ring-opening by H₂O which takes place already at ≥ 40 °C. Thus, the study underlines the advantages of organo-silicon compounds as electrolyte additives. Elucidating the reaction mechanism in model systems like this is important for future studies of similar additives, in order to improve the accuracy of additive exploration in LIBs.

In general, water is always brought in to cell with every cell component because of the difficulty to perfectly dry these components. The water content can easily reach hundreds of ppm. The challenge with water is that it triggers autocatalytic decomposition reactions with the electrolyte solvents and salts. This is where VC and TMSPa come in to neutralize both H₂O and LBs such as LiOH.

Looking forward, investigating the chemical and electrochemical reactions during nanometric electrode/electrolyte interphase formation will continue to be a challenging task. *Operando* SERS, gas analysis and NMR are however powerful techniques to study this phenomenon owing to their high sensitivity and selectivity. Cell contaminants, even in low concentrations, complicates these studies and has to be accounted for. Hence, studies involving the meticulous approach of adding known amounts of contaminants to understand their influence on the interphase formation processes have to be undertaken.

Understanding the formation and decomposition reaction pathways fundamentally provides valuable insights for designing successful mitigation strategies. This could involve for example, incorporating a water-scavenging electrolyte additive or separator, as well as designing coatings to prevent such adverse reactions. By pinpointing decomposition products and their formation mechanism, future research can explore their impact on electrode crosstalk processes, potentially enhancing our comprehension of parasitic reactions at the negative electrode that diminish the battery's lifespan.

6 Sammanfattning på Svenska

Ett kemiskt stabilt, tunt och passiverande lager ("Solid electrolyte interphase, SEI") på ytan av den negativa elektroden är en förutsättning för ett välfungerande litiumjonbatteri (LIB). Det finns dock ingen konsensus kring bildningsmekanismen av detta SEI lager och dess sammansättning eller struktur. I litteraturen har modeller presenterats som sträcker sig från strukturer baserade på en- till flerskiktsslager samt heterogena strukturer, men valideringsexperiment av dessa modeller är utmanande och resultaten tvetydiga.

I denna avhandling har en modell av ett förenklat elektrospektroskopiskt system tillämpats för att studera den komplexa SEI-bildningsmekanismen i ett LIB. För att isolera den reducerande effekten av etylenkarbonat (EC) används denna i en elektrolyt baserad på LiClO_4 och med guld som arbetelektrod. Den stegvisa elektrokemiska reduktionen av elektrolytens beståndsdelar under SEI-bildning i detta modellsystem studerades med *Operando* ytförstärkt Raman-spektroskopi kompletterat med online-elektrokemiskt masspektrometri. Olika elektrokemiska ytprocesser, såsom lösningsmedelsreduktion samt elektrod- och elektrolytföroreningar har visats spela en betydande roll i SEI-uppbyggnaden. Föroreningar såsom vatten samt föroreningar som innehåller kol och syre (som O_2 och CO_2) har visat sig störa SEI-bildningsmekanismen. Oavsett elektrolytsammansättning är litiumkarbonat och litiumoxid de dominerande beståndsdelarna i SEI. Detta avslöjas av SERS som visar deras uppkomst redan vid 2 V mot Li^+/Li . Ytterligare fenomen associerade med elektrisk dubbelskiktssladdning, elektrodadsorberande polarisering (Stark effekt) och SEI-upplösning har analyserats. Dessa analysmetoder ger djupare insikter i de underliggande mekanismerna, däremot finns det fortfarande begränsningar. Tekniken är till exempel som mest effektiv när molekylen interagerar starkt med substratet.

Additiv i låga koncentrationer tillsätts i elektrolyten för att förbättra prestandan på batteriet. Dessa är funktionella molekyler såsom VC, som finns i nästan alla kommersiella LIB. Denna tillsats formar SEI och reduceras innan elektrolyten över 1 V mot Li^+/Li på den negativa elektroden samt undertrycker senare nedbrytning av EC. VC har inte bara visat sig polymerisera och bilda poly(vylenkarbonat) som skyddar elektrodytan, utan också frigöra stora mängder CO_2 , vilket är två till synes motstridiga processer. Bildningsmekanismen för CO_2 från VC-nedbrytning i elektrolyt har studerats grundligt i ett

försök att förstå dess implikation på SEI-bildningsprocesserna. Det konstateras att stora mängder CO₂ genereras när VC är närvarande. Detta beror på att aktiveringsenergin för nedbrytning av VC för att producera CO₂ är lägre än dess mättade motsvarighet, EC. Det första steget i denna VC-nedbrytningsprocess är ringöppningen som snarare är en kemiskt aktiverad process via till exempel hydrolys av VC. Detta resulterar även i en blandning av olika lösliga polymera/oligomera kedjefragment som detekteras med vätske-NMR.

Vid låga elektropotentialer kan CO₂ som bildas från VC-nedbrytning reduceras till litiumformat som så småningom kan bidra till SEI. VC har även visats undertrycka H₂-utvecklingen i LIB. Detta tillskrivs den snabbare ringöppningen av VC jämfört med EC som därefter förbrukar H₂O. Denna hypotes bevisades genom Karl-Fischer-titrering utförd på ett lösningsmedel som var avsiktligt förorenat med vatten till vilket VC tillsattes med och utan hydroxid. Dessutom har det också visats i denna avhandling att VC kan abstrahera reducerade protoner från ytan av den negativa elektroden och omvandlas till EC. En viktig funktion hos VC är alltså att den leder till ett tunnare SEI genom att undertrycka H₂O-reduktion.

I den senare delen av avhandlingen undersöks reaktiviteten hos Lewis-baser, som vanligtvis finns i SEI, mot olika elektrolytlösningsmedel. Tris(trimetylsilyl)-fosfat (TMSPa), en välkänd representant för organokiselbaserade elektrolyttillsatser, har använts för att kemiskt undersöka dess reaktivitet och den underliggande reaktionsmekanismen. TMSPa anses fungera som multifunktionella molekyler: fluoridrensare och bilda passiverande lager på den positiva elektroden i LIB. Genom att kombinera *in-situ* headspace-gasanalys och konventionell vätske-NMR för att kvalitativt analysera reaktionsprodukterna kunde följande slutsatser dras. Lewis-baser är potentiellt skadliga eftersom de leder till elektrolytnedbrytning i cellen. Att inkludera TMSPa i små koncentrationer är effektivt för att rensa bort dessa Lewis-baser samtidigt som de ersätts med mindre skadliga och elektrolytlösliga trimetylsilylbaserade komponenter. Tillsatsen får sin huvudsakliga funktion från dess kisel-syrebinding. Intermolekylära fysikalisk-kemiska effekter, såsom anjonmottagning kommer sannolikt att vara mycket viktiga men förbli ett ämne för framtida studier.

Uppföljningsstudien betonade reaktiviteten av TMSPa med vatten i konventionella organiska karbonatlösningsmedel. De huvudsakliga reaktionsprodukterna identifierades som trimetylsilanol (TMSOH) och fosforsyra (H₃PO₄), samt olika P–O–Si-innehållande intermediära molekyler. TMSOH, en Lewis-bas, kan på samma sätt som vatten genomgå reaktion med TMSPa vid rumstemperatur för att bilda hexametyldisiloxan (TMSOTMS) och kan även aktivera ringöppningsreaktionen av EC vid förhöjda temperaturer (≥ 80 °C) vilket resulterar i derivat så som etylenglykol (TMS-EG). Även om uppkomsten av TMS-EG på bekostnad av EC är en oönskad parasitreaktion, bör det noteras att denna reaktion endast aktiveras vid förhöjda temperaturer i jämförelse med EC-ringöppning av H₂O som redan äger rum vid ≥ 40 °C. Således

understryker studien fördelarna med organiska kiselföreningar som elektrolyttillsatser. Att belysa reaktionsmekanismen i modellsystem som detta är viktigt för framtida studier av liknande tillsatser, för en mer noggrann och förbättrad kartläggning av tillsatser i LIB.

I allmänhet förs vatten alltid in i cellen med varje cellkomponent på grund av svårigheten att fullkomligt torka dessa komponenter. Vattenhalten kan lätt nå hundratals ppm. Utmaningen med vatten är att det utlöser autocatalytiska nedbrytningsreaktioner med elektrolytlösningsmedel och salter. Det är här VC och TMSPa kommer in för att neutralisera både H_2O och LB som $LiOH$.

Under de kommande åren fortsätter utmaningen med att undersöka kemiska och elektrokemiska reaktioner vid elektrod/elektrolyt-interfasbildning. Under de kommande åren kommer det att fortsätta att vara en utmanande uppgift att undersöka de kemiska och elektrokemiska reaktionerna vid elektrod/elektrolyt-interfasbildning. *Operando* SERS, *in-situ* masspektrometri och NMR är dock kraftfulla tekniker för att studera dessa processer på grund av deras höga känslighet och selektivitet. Föreningar, även i låga koncentrationer, komplicerar dessa studier och måste beaktas.

Därför kan noggranna studier som dessa, där kända mängder föreningar tillsätts, påvisa deras inverkan på de processer som sker vid interfasbildning. Att förstå reaktionsvägarna för bildning och nedbrytning ger i grunden värdefulla insikter för att utforma framgångsrika strategier som begränsar negativa effekter. Detta kan exempelvis involvera att tillsätta en vattenabsorberande elektrolyttillsats eller separator, såväl som att utforma beläggningar för att förhindra negativa reaktioner. Genom att fastställa nedbrytningsprodukter och deras bildningsmekanism kan framtida forskning kartlägga deras inverkan på korskontaminering mellan elektroder, vilket potentiellt kan förbättra vår förståelse av reaktioner som förkortar batteriets livslängd.

7 Acknowledgements

First and foremost, I would like to acknowledge and give my warmest thanks to my supervisor and mentor, Erik. I appreciate all the opportunities and guidance you have given me in this journey. Thank you for showing the faith in me always. I know the road was not smooth, but that's what makes it so special. And Guiomar, thank you for being so supportive, understanding and patient with me. I could not have asked for better mentors and advisors. I wish to express my gratitude to Daniel for giving feedbacks when needed. I am eternally indebted to our Amazing *#InterphaseTeam* for all the discussions, meetings, kick-offs and feedback sessions. I have learned a lot more from those than I could describe in words. A special shoutout to Robin, Tim, Kaz, Jackie and Xu, working together was so much enjoyable. Thanks to Peter for all the discussions, you always ask the right question! Thanks to the bigger structural chemistry family for everything. Thanks to the NMR facility (especially to Rui) in BMC. A massive thanks to all my collaborators. Working together was very fun. Wasn't it? :-p

I wish to thank everyone for all the fikas and meals that we all have had together. Heyin and Souzan, you have been the greatest friend inside and outside of Ångström. Thanks Tim and Souzan for helping with my 'Sammanfattning'. Thanks to our lab and lab equipment responsible. I would not have been able to complete this thesis without all your efforts.

I would like to express my gratitude to all the teachers, friends, and colleagues whom I've encountered, worked with, and spent time with from my formative years until now. I appreciate each and every individual I've crossed paths with; you have made an impact in ways you may not even be aware of.

Last but certainly not least, a special thanks to my significant other, Nipon, for being always there through thick and thin. Your turn is up next! Thanks to Ma, Deuta and my sisters, Hanna and Thunu, for giving me reality checks from time to time.

Life is a lot more meaningful when you have such good people around who keeps you grounded.

Thank you for taking the time to read this. You're AWESOME!

"I'd like to thank my laptop for always being there especially during the darkest hours of thesis writing. You're the real MVP."

8 References

- (1) Gogoi, N.; Melin, T.; Berg, E. J. Elucidating the Step-Wise Solid Electrolyte Interphase Formation in Lithium-Ion Batteries with Operando Raman Spectroscopy. *Adv. Mater. Interfaces* **2022**, 2200945.
- (2) Gogoi, N.; Bowall, E.; Lundström, R.; Mozhzhukhina, N.; Hernández, G.; Broqvist, P.; Berg, E. J. Silyl-Functionalized Electrolyte Additives and Their Reactivity toward Lewis Bases in Li-Ion Cells. *Chem. Mater.* **2022**, 34 (8), 3831–3838. <https://doi.org/10.1021/acs.chemmater.2c00345>.
- (3) Gogoi, N.; Wahyudi, W.; Mindemark, J.; Hern, G.; Broqvist, P.; Berg, E. J. Reactivity of Organosilicon Additives with Water in Li-Ion Batteries. **2024**. <https://doi.org/10.1021/acs.jpcc.3c07505>.
- (4) Lundström, R.; Gogoi, N.; Hou, X.; Berg Erik J. Competing Ethylene Carbonate Reactions on Carbon Electrode in Li-Ion Batteries. *J. Electrochem. Soc.* **2023**, No. 170, 040516. <https://doi.org/10.1149/1945-7111/accb6e>.
- (5) Hou, X.; Zhang, L.; Gogoi, N.; Edström, K.; Berg, E. J. Interfacial Chemistry in Aqueous Lithium-Ion Batteries: A Case Study of V2O5 in Dilute Aqueous Electrolytes. *Small* **2023**, 2308577, 1–8. <https://doi.org/10.1002/sml.202308577>.
- (6) Yang, Z.; Zhang, J.; Kintner-Meyer, M. C. W.; Lu, X.; Choi, D.; Lemmon, J. P.; Liu, J. Electrochemical Energy Storage for Green Grid. *Chem. Rev.* **2011**, 111 (5), 3577–3613. <https://doi.org/10.1021/cr100290v>.
- (7) Xu, K. Nonaqueous Liquid Electrolytes for Lithium-Based Rechargeable Batteries. *Chem. Rev.* **2004**, 104 (10), 4303–4417. <https://doi.org/10.1021/cr030203g>.
- (8) M. S. Whittingham. Electrical Energy Storage and Intercalation Chemistry Abstract. *Science* (80-.). **1976**, 192 (4244). <https://doi.org/10.1126/science.192.4244.1126>.
- (9) Feng, K.; Li, M.; Liu, W.; Kashkooli, A. G.; Xiao, X.; Cai, M.; Chen, Z. Silicon-Based Anodes for Lithium-Ion Batteries: From Fundamentals to Practical Applications. *Small*. Wiley-VCH Verlag February 22, **2018**. <https://doi.org/10.1002/sml.201702737>.
- (10) Nishi, Y. Lithium Ion Secondary Batteries; Past 10 Years and the Future. *J. Power Sources* **2001**, 100 (1–2), 101–106. [https://doi.org/10.1016/S0378-7753\(01\)00887-4](https://doi.org/10.1016/S0378-7753(01)00887-4).
- (11) Luo, W.; Cheng, S.; Wu, M.; Zhang, X.; Yang, D.; Rui, X. A Review of Advanced Separators for Rechargeable Batteries. *J. Power Sources* **2021**, 509 (August), 230372. <https://doi.org/10.1016/j.jpowsour.2021.230372>.
- (12) Campion, C. L.; Li, W.; Lucht, B. L. Thermal Decomposition of LiPF[Sub 6]-Based Electrolytes for Lithium-Ion Batteries. *J. Electrochem. Soc.* **2005**, 152 (12), A2327. <https://doi.org/10.1149/1.2083267>.
- (13) Tan, J.; Matz, J.; Dong, P.; Shen, J.; Ye, M. A Growing Appreciation for the Role of LiF in the Solid Electrolyte Interphase. *Adv. Energy Mater.* **2021**, 11 (16), 1–25. <https://doi.org/10.1002/aenm.202100046>.

- (14) Huey, Z.; Ha, Y.; Frisco, S.; Norman, A.; Teeter, G.; Jiang, C. S.; DeCaluwe, S. C. Multi-Modal Characterization Methods of Solid-Electrolyte Interphase in Silicon-Graphite Composite Electrodes. *J. Power Sources* **2023**, *564* (January), 232804. <https://doi.org/10.1016/j.jpowsour.2023.232804>.
- (15) Erickson, E. M.; Schipper, F.; Penki, T. R.; Shin, J.-Y.; Erk, C.; Chesneau, F.-F.; Markovsky, B.; Aurbach, D. Review—Recent Advances and Remaining Challenges for Lithium Ion Battery Cathodes. *J. Electrochem. Soc.* **2017**, *164* (1), A6341–A6348. <https://doi.org/10.1149/2.0461701jes>.
- (16) Xu, K. Electrolytes and Interphases in Li-Ion Batteries and Beyond. *Chem. Rev.* **2014**, *114* (23), 11503–11618. <https://doi.org/10.1021/cr500003w>.
- (17) Zhang, Q. K.; Zhang, X. Q.; Yuan, H.; Huang, J. Q. Thermally Stable and Nonflammable Electrolytes for Lithium Metal Batteries: Progress and Perspectives. *Small Sci.* **2021**, *1* (10). <https://doi.org/10.1002/smssc.202100058>.
- (18) Nie, M.; Abraham, D. P.; Chen, Y.; Bose, A.; Lucht, B. L. Lithium Ion Battery Graphite Solid Electrolyte Interphase Revealed by Microscopy and Spectroscopy. *J. Phys. Chem. C* **2013**, *117* (26), 13403–13412. <https://doi.org/10.1021/jp404155y>.
- (19) Wang, Y.; Nakamura, S.; Ue, M.; Balbuena, P. B. Theoretical Studies to Understand Surface Chemistry on Carbon Anodes for Lithium-Ion Batteries: Reduction Mechanisms of Ethylene Carbonate. *J. Am. Chem. Soc.* **2001**, *123* (47), 11708–11718. <https://doi.org/10.1021/ja0164529>.
- (20) Adams, B. D.; Black, R.; Williams, Z.; Fernandes, R.; Cuisinier, M.; Berg, E. J.; Novak, P.; Murphy, G. K.; Nazar, L. F. Towards a Stable Organic Electrolyte for the Lithium Oxygen Battery. *Adv. Energy Mater.* **2015**, *5* (1), 1–11. <https://doi.org/10.1002/aenm.201400867>.
- (21) Wang, D. Y.; Dahn, J. R. A High Precision Study of Electrolyte Additive Combinations Containing Vinylene Carbonate, Ethylene Sulfate, Tris(Trimethylsilyl) Phosphate and Tris(Trimethylsilyl) Phosphite in Li[Ni 1/3 Mn 1/3 Co 1/3]O 2 /Graphite Pouch Cells . *J. Electrochem. Soc.* **2014**, *161* (12), A1890–A1897. <https://doi.org/10.1149/2.0841412jes>.
- (22) Petibon, R.; Xia, J.; Burns, J. C.; Dahn, J. R. Study of the Consumption of Vinylene Carbonate in Li[Ni 0.33 Mn 0.33 Co 0.33]O 2 /Graphite Pouch Cells . *J. Electrochem. Soc.* **2014**, *161* (10), A1618–A1624. <https://doi.org/10.1149/2.0351410jes>.
- (23) Aurbach, D.; Gamolsky, K.; Markovsky, B.; Gofer, Y.; Schmidt, M.; Heider, U. On the Use of Vinylene Carbonate (VC) as an Additive to Electrolyte Solutions for Li-Ion Batteries. *Electrochim. Acta* **2002**, *47* (9), 1423–1439. [https://doi.org/10.1016/S0013-4686\(01\)00858-1](https://doi.org/10.1016/S0013-4686(01)00858-1).
- (24) Ota, H.; Sakata, Y.; Inoue, A.; Yamaguchi, S. Analysis of Vinylene Carbonate Derived SEI Layers on Graphite Anode. *J. Electrochem. Soc.* **2004**, *151* (10), A1659. <https://doi.org/10.1149/1.1785795>.
- (25) Grugeon, S.; Jankowski, P.; Cailleu, D.; Forestier, C.; Sannier, L.; Armand, M.; Johansson, P.; Laruelle, S. Towards a Better Understanding of Vinylene Carbonate Derived SEI-Layers by Synthesis of Reduction Compounds. *J. Power Sources* **2019**, *427* (April), 77–84. <https://doi.org/10.1016/j.jpowsour.2019.04.061>.
- (26) Kamikawa, Y.; Amezawa, K.; Terada, K. First-Principles Study on the Mechanical Properties of Polymers Formed by the Electrochemical Reduction of Fluoroethylene Carbonate and Vinylene Carbonate. *J. Phys. Chem. C* **2020**, *124* (37), 19937–19944. <https://doi.org/10.1021/acs.jpcc.0c04878>.

- (27) El Ouatani, L.; Dedryvère, R.; Siret, C.; Biensan, P.; Reynaud, S.; Iratçabal, P.; Gonbeau, D. The Effect of Vinylene Carbonate Additive on Surface Film Formation on Both Electrodes in Li-Ion Batteries. *J. Electrochem. Soc.* **2009**, *156* (2), A103. <https://doi.org/10.1149/1.3029674>.
- (28) Soto, F. A.; Ma, Y.; Martinez De La Hoz, J. M.; Seminario, J. M.; Balbuena, P. B. Formation and Growth Mechanisms of Solid-Electrolyte Interphase Layers in Rechargeable Batteries. *Chem. Mater.* **2015**, *27* (23), 7990–8000. <https://doi.org/10.1021/acs.chemmater.5b03358>.
- (29) Kim, D. Y.; Park, H.; Choi, W. I.; Roy, B.; Seo, J.; Park, I.; Kim, J. H.; Park, J. H.; Kang, Y. S.; Koh, M. Ab Initio Study of the Operating Mechanisms of Tris(Trimethylsilyl) Phosphite as a Multifunctional Additive for Li-Ion Batteries. *J. Power Sources* **2017**, *355*, 154–163. <https://doi.org/10.1016/j.jpowsour.2017.04.062>.
- (30) Han, J. G.; Hwang, E.; Kim, Y.; Park, S.; Kim, K.; Roh, D. H.; Gu, M.; Lee, S. H.; Kwon, T. H.; Kim, Y.; Choi, N. S.; Kim, B. S. Dual-Functional Electrolyte Additives toward Long-Cycling Lithium-Ion Batteries: Ecofriendly Designed Carbonate Derivatives. *ACS Appl. Mater. Interfaces* **2020**, *12* (21), 24479–24487. <https://doi.org/10.1021/acsami.0c04372>.
- (31) Guéguen, A.; Bolli, C.; Mendez, M. A.; Berg, E. J. Elucidating the Reactivity of Tris(Trimethylsilyl)Phosphite and Tris(Trimethylsilyl)Phosphate Additives in Carbonate Electrolytes - A Comparative Online Electrochemical Mass Spectrometry Study. *ACS Appl. Energy Mater.* **2020**, *3* (1), 290–299. <https://doi.org/10.1021/acsaem.9b01551>.
- (32) Peebles, C.; Sahore, R.; Gilbert, J. A.; Garcia, J. C.; Tornheim, A.; Bareño, J.; Iddir, H.; Liao, C.; Abraham, D. P. Tris(Trimethylsilyl) Phosphite (TMSPi) and Triethyl Phosphite (TEPi) as Electrolyte Additives for Lithium Ion Batteries: Mechanistic Insights into Differences during LiNi 0.5 Mn 0.3 Co 0.2 O 2 -Graphite Full Cell Cycling. *J. Electrochem. Soc.* **2017**, *164* (7), A1579–A1586. <https://doi.org/10.1149/2.1101707jes>.
- (33) Peebles, C.; Garcia, J.; Tornheim, A. P.; Sahore, R.; Bareño, J.; Liao, C.; Shkrob, I. A.; Iddir, H. H.; Abraham, D. P. Chemical “Pickling” of Phosphite Additives Mitigates Impedance Rise in Li Ion Batteries. *J. Phys. Chem. C* **2018**, *122* (18), 9811–9824. <https://doi.org/10.1021/acs.jpcc.8b02056>.
- (34) Bolli, C.; Guéguen, A.; Mendez, M. A.; Berg, E. J. Operando Monitoring of F - Formation in Lithium Ion Batteries. *Chem. Mater.* **2019**, *31* (4), 1258–1267. <https://doi.org/10.1021/acs.chemmater.8b03810>.
- (35) Bolli, C.; Guéguen, A.; Mendez, M. A.; Berg, E. J. Operando Monitoring of F - Formation in Lithium Ion Batteries. *Chem. Mater.* **2019**, *31* (4), 1258–1267. <https://doi.org/10.1021/acs.chemmater.8b03810>.
- (36) Xu, K. Interfaces and Interphases in Batteries. *J. Power Sources* **2023**, *559* (January), 232652. <https://doi.org/10.1016/j.jpowsour.2023.232652>.
- (37) Peled, E. The Electrochemical Behavior of Alkali and Alkaline Earth Metals in Nonaqueous Battery Systems—The Solid Electrolyte Interphase Model. *J. Electrochem. Soc.* **1979**, *126* (12), 2047–2051. <https://doi.org/10.1149/1.2128859>.
- (38) Qian, Y.; Niehoff, P.; Börner, M.; Grütze, M.; Mönnighoff, X.; Behrends, P.; Nowak, S.; Winter, M.; Schappacher, F. M. Influence of Electrolyte Additives on the Cathode Electrolyte Interphase (CEI) Formation on LiNi1/3Mn1/3Co1/3O2 in Half Cells with Li Metal Counter Electrode. *J. Power Sources* **2016**, *329*, 31–40. <https://doi.org/10.1016/j.jpowsour.2016.08.023>.

- (39) Bockris, J. O. M., Reddy, A. K. N., & Gamboa-Aldeco, M. E. *Modern Electrochemistry: Fundamentals of Electrodics*; **1998**; Vol. 2a.
- (40) Aurbach, D.; Markovsky, B.; Shechter, A.; Ein-Eli, Y.; Cohen, H. A Comparative Study of Synthetic Graphite and Li Electrodes in Electrolyte Solutions Based on Ethylene Carbonate-Dimethyl Carbonate Mixtures. *J. Electrochem. Soc.* **1996**, *143* (12), 3809–3820. <https://doi.org/10.1149/1.1837300>.
- (41) Xie, X.; Clark Spotte-Smith, E. W.; Wen, M.; Patel, H. D.; Blau, S. M.; Persson, K. A. Data-Driven Prediction of Formation Mechanisms of Lithium Ethylene Monocarbonate with an Automated Reaction Network. *J. Am. Chem. Soc.* **2021**, *143* (33), 13245–13258. <https://doi.org/10.1021/jacs.1c05807>.
- (42) Aurbach, D. *Nonaqueous Electrochemistry by Doron Aurbach*; **1999**.
- (43) Metzger, M.; Strehle, B.; Solchenbach, S.; Gasteiger, H. A. Hydrolysis of Ethylene Carbonate with Water and Hydroxide under Battery Operating Conditions. *J. Electrochem. Soc.* **2016**, *163* (7), A1219–A1225. <https://doi.org/10.1149/2.0411607jes>.
- (44) Kitz, P. G.; Novák, P.; Berg, E. J. Influence of Water Contamination on the SEI Formation in Li-Ion Cells: An Operando EQCM-D Study. *ACS Appl. Mater. Interfaces* **2020**, *12* (13), 15934–15942. <https://doi.org/10.1021/acsami.0c01642>.
- (45) Winter, M. The Solid Electrolyte Interphase - The Most Important and the Least Understood Solid Electrolyte in Rechargeable Li Batteries. *Zeitschrift für Phys. Chemie* **2009**, *223* (10–11), 1395–1406. <https://doi.org/10.1524/zpch.2009.6086>.
- (46) Peled, E. Film Forming Reaction at the Lithium/Electrolyte Interface. *J. Power Sources* **1983**, *9* (3), 253–266. [https://doi.org/10.1016/0378-7753\(83\)87026-8](https://doi.org/10.1016/0378-7753(83)87026-8).
- (47) Zaban, A.; Aurbach, D. Impedance Spectroscopy of Lithium and Nickel Electrodes in Propylene Carbonate Solutions of Different Lithium Salts A Comparative Study. *J. Power Sources* **1995**, *54* (2), 289–295. [https://doi.org/10.1016/0378-7753\(94\)02086-1](https://doi.org/10.1016/0378-7753(94)02086-1).
- (48) Peled, E.; Golodnitsky, D.; Ardel, G. Advanced Model for Solid Electrolyte Interphase Electrodes in Liquid and Polymer Electrolytes. *J. Electrochem. Soc.* **1997**, *144* (8), L208–L210. <https://doi.org/10.1149/1.1837858>.
- (49) Ein-Eli, Y. New Perspective on the Foundation and Structure of the Solid Electrolyte Interface at the Graphite Anode of Li-Ion Cells. *Electrochem. Solid-State Lett.* **1999**, *2* (5), 212–214. <https://doi.org/10.1149/1.1390787>.
- (50) Edström, K.; Herstedt, M.; Abraham, D. P. A New Look at the Solid Electrolyte Interphase on Graphite Anodes in Li-Ion Batteries. *J. Power Sources* **2006**, *153* (2), 380–384. <https://doi.org/10.1016/j.jpowsour.2005.05.062>.
- (51) Andersson, A. M.; Edström, K. Chemical Composition and Morphology of the Elevated Temperature SEI on Graphite. *J. Electrochem. Soc.* **2001**, *148* (10), A1100. <https://doi.org/10.1149/1.1397771>.
- (52) Verma, P.; Maire, P.; Novák, P. A Review of the Features and Analyses of the Solid Electrolyte Interphase in Li-Ion Batteries. *Electrochim. Acta* **2010**, *55* (22), 6332–6341. <https://doi.org/10.1016/j.electacta.2010.05.072>.
- (53) Powers, P. E. Raman Microscopy. *F. Guid. to Nonlinear Opt.* **2013**. <https://doi.org/10.1117/3.1002081.ch62>.
- (54) Langer, J.; de Aberasturi, D. J.; Aizpurua, J.; Alvarez-Puebla, R. A.; Auguie, B.; Baumberg, J. J.; Bazan, G. C.; Bell, S. E. J.; Boisen, A.; Brolo, A. G.; Choo, J.; Cialla-May, D.; Deckert, V.; Fabris, L.; Faulds, K.; Javier García de Abajo, F.; Goodacre, R.; Graham, D.; Haes, A. J.; Haynes, C. L.; Huck, C.; Itoh, T.;

- Käll, M.; Kneipp, J.; Kotov, N. A.; Kuang, H.; Le Ru, E. C.; Lee, H. K.; Li, J. F.; Ling, X. Y.; Maier, S. A.; Mayerhöfer, T.; Moskovits, M.; Murakoshi, K.; Nam, J. M.; Nie, S.; Ozaki, Y.; Pastoriza-Santos, I.; Perez-Juste, J.; Popp, J.; Pucci, A.; Reich, S.; Ren, B.; Schatz, G. C.; Shegai, T.; Schlücker, S.; Tay, L. L.; George Thomas, K.; Tian, Z. Q.; van Duyne, R. P.; Vo-Dinh, T.; Wang, Y.; Willets, K. A.; Xu, C.; Xu, H.; Xu, Y.; Yamamoto, Y. S.; Zhao, B.; Liz-Marzán, L. M. Present and Future of Surface-Enhanced Raman Scattering. *ACS Nano* **2020**, *14* (1), 28–117. <https://doi.org/10.1021/acsnano.9b04224>.
- (55) Le Ru, E. C.; Blackie, E.; Meyer, M.; Etchegoint, P. G. Surface Enhanced Raman Scattering Enhancement Factors: A Comprehensive Study. *J. Phys. Chem. C* **2007**, *111* (37), 13794–13803. <https://doi.org/10.1021/jp0687908>.
- (56) Michaels, A. M.; Nirmal, M.; Brus, L. E. Surface Enhanced Raman Spectroscopy of Individual Rhodamine 6G Molecules on Large Ag Nanocrystals. *J. Am. Chem. Soc.* **1999**, *121* (43), 9932–9939. <https://doi.org/10.1021/ja992128q>.
- (57) Ha, Y.; Villers, B. J. T. De; Li, Z.; Xu, Y.; Stradins, P.; Zakutayev, A.; Burrell, A.; Han, S. Probing the Evolution of Surface Chemistry at the Silicon – Electrolyte Interphase via In Situ Surface-Enhanced Raman Spectroscopy. **2020**. <https://doi.org/10.1021/acs.jpcclett.9b03284>.
- (58) Mozhzhukhina, N.; Flores, E.; Lundström, R.; Nystrom, V.; Kitz, P. G.; Edström, K.; Berg, E. J. Direct Operando Observation of Double Layer Charging and Early SEI Formation in Li-Ion Battery Electrolytes. *ChemRxiv* **2020**, 1–7. <https://doi.org/10.26434/chemrxiv.12091713.v1>.
- (59) Hy, S.; Felix; Chen, Y. H.; Liu, J. Y.; Rick, J.; Hwang, B. J. In Situ Surface Enhanced Raman Spectroscopic Studies of Solid Electrolyte Interphase Formation in Lithium Ion Battery Electrodes. *J. Power Sources* **2014**, *256*, 324–328. <https://doi.org/10.1016/j.jpowsour.2014.01.092>.
- (60) Gajan, A.; Lecourt, C.; Torres Bautista, B. E.; Fillaud, L.; Demeaux, J.; Lucas, I. T. Solid Electrolyte Interphase Instability in Operating Lithium-Ion Batteries Unraveled by Enhanced-Raman Spectroscopy. *ACS Energy Lett.* **2021**, 1757–1763. <https://doi.org/10.1021/acsenenergylett.1c00436>.
- (61) Rinkel, B. L. D.; Hall, D. S.; Temprano, I.; Grey, C. P. Electrolyte Oxidation Pathways in Lithium-Ion Batteries. *J. Am. Chem. Soc.* **2020**, *142* (35), 15058–15074. <https://doi.org/10.1021/jacs.0c06363>.
- (62) Wang, L.; Menakath, A.; Han, F.; Wang, Y.; Zavalij, P. Y.; Gaskell, K. J.; Borodin, O.; Iuga, D.; Brown, S. P.; Wang, C.; Xu, K.; Eichhorn, B. W. Identifying the Components of the Solid–Electrolyte Interphase in Li-Ion Batteries. *Nat. Chem.* **2019**, *11* (9), 789–796. <https://doi.org/10.1038/s41557-019-0304-z>.
- (63) Von Seggern, N.; Schindler, T.; Naumann, S. Dual Catalytic Ring-Opening Polymerization of Ethylene Carbonate for the Preparation of Degradable PEG. *Biomacromolecules* **2020**, *21* (7), 2661–2669. <https://doi.org/10.1021/acs.biomac.0c00360>.
- (64) Lundström, R.; Berg, E. J. Design and Validation of an Online Partial and Total Pressure Measurement System for Li-Ion Cells. *J. Power Sources* **2021**, 485 (November 2020). <https://doi.org/10.1016/j.jpowsour.2020.229347>.
- (65) Kitz, P. G.; Lacey, M. J.; Novák, P.; Berg, E. J. Operando Investigation of the Solid Electrolyte Interphase Mechanical and Transport Properties Formed from Vinylene Carbonate and Fluoroethylene Carbonate. *J. Power Sources* **2020**, 477 (June), 0–8. <https://doi.org/10.1016/j.jpowsour.2020.228567>.

- (66) Schmidt, M. S.; Hübner, J.; Boisen, A. Large Area Fabrication of Leaning Silicon Nanopillars for Surface Enhanced Raman Spectroscopy. *Adv. Mater.* **2012**, *24* (10), 11–18. <https://doi.org/10.1002/adma.201103496>.
- (67) Chau, V. K. C.; Chen, Z.; Hu, H.; Chan, K.-Y. Exploring Solvent Stability against Nucleophilic Attack by Solvated LiO² – in an Aprotic Li-O² Battery. *J. Electrochem. Soc.* **2017**, *164* (2), A284–A289. <https://doi.org/10.1149/2.0961702jes>.
- (68) Freunberger, S. A.; Chen, Y.; Peng, Z.; Griffin, J. M.; Hardwick, L. J.; Bardé, F.; Novák, P.; Bruce, P. G. Reactions in the Rechargeable Lithium-O₂ Battery with Alkyl Carbonate Electrolytes. *J. Am. Chem. Soc.* **2011**, *133* (20), 8040–8047. <https://doi.org/10.1021/ja2021747>.
- (69) Radjenovic, P. M.; Hardwick, L. J. Time-Resolved SERS Study of the Oxygen Reduction Reaction in Ionic Liquid Electrolytes for Non-Aqueous Lithium-Oxygen Cells. *Faraday Discuss.* **2018**, *206*, 379–392. <https://doi.org/10.1039/c7fd00170c>.
- (70) Moradzaman, M.; Mul, G. In Situ Raman Study of Potential-Dependent Surface Adsorbed Carbonate, CO, OH, and C Species on Cu Electrodes During Electrochemical Reduction of CO₂. *ChemElectroChem* **2021**, *8* (8), 1478–1485. <https://doi.org/10.1002/celc.202001598>.
- (71) Calaza, F.; Stiehler, C.; Fujimori, Y.; Sterrer, M.; Beeg, S.; Ruiz-Oses, M.; Nilius, N.; Heyde, M.; Parviainen, T.; Honkala, K.; Häkkinen, H.; Freund, H. J. Carbon Dioxide Activation and Reaction Induced by Electron Transfer at an Oxide-Metal Interface. *Angew. Chemie - Int. Ed.* **2015**, *54* (42), 12484–12487. <https://doi.org/10.1002/anie.201501420>.
- (72) Tang, M.; Lu, S.; Newman, J. Experimental and Theoretical Investigation of Solid-Electrolyte-Interphase Formation Mechanisms on Glassy Carbon. *J. Electrochem. Soc.* **2012**, *159* (11), A1775–A1785. <https://doi.org/10.1149/2.025211jes>.
- (73) Schwenke, K. U.; Solchenbach, S.; Demeaux, J.; Lucht, B. L.; Gasteiger, H. A. The Impact of CO₂ Evolved from VC and FEC during Formation of Graphite Anodes in Lithium-Ion Batteries. *J. Electrochem. Soc.* **2019**, *166* (10), A2035–A2047. <https://doi.org/10.1149/2.0821910jes>.
- (74) Metzger, M.; Strehle, B.; Solchenbach, S.; Gasteiger, H. A. Origin of H₂ Evolution in LIBs: H₂O Reduction vs. Electrolyte Oxidation. *J. Electrochem. Soc.* **2016**, *163* (5), A798–A809. <https://doi.org/10.1149/2.1151605jes>.
- (75) Metzger, M.; Strehle, B.; Solchenbach, S.; Gasteiger, H. A. Hydrolysis of Ethylene Carbonate with Water and Hydroxide under Battery Operating Conditions. *J. Electrochem. Soc.* **2016**, *163* (7), A1219–A1225. <https://doi.org/10.1149/2.0411607jes>.
- (76) Bernhard, R.; Metzger, M.; Gasteiger, H. A. Gas Evolution at Graphite Anodes Depending on Electrolyte Water Content and SEI Quality Studied by On-Line Electrochemical Mass Spectrometry. *J. Electrochem. Soc.* **2015**, *162* (10), A1984–A1989. <https://doi.org/10.1149/2.0191510jes>.
- (77) Aurbach, D.; Daroux, M. L.; Faguy, P. W.; Yeager, E. Identification of Surface Films Formed on Lithium in Propylene Carbonate Solutions. *J. Electrochem. Soc.* **1987**, *134* (7), 1611–1620. <https://doi.org/10.1149/1.2100722>.
- (78) Zhuang, G. V.; Ross, P. N. Analysis of the Chemical Composition of the Passive Film on Li-Ion Battery Anodes Using Attenuated Total Reflection Infrared Spectroscopy. *Electrochem. Solid-State Lett.* **2003**, *6* (7). <https://doi.org/10.1149/1.1575594>.

- (79) Tasaki, K.; Harris, S. J. Computational Study on the Solubility of Lithium Salts Formed on Lithium Ion Battery Negative Electrode in Organic Solvents. *J. Phys. Chem. C* **2010**, *114* (17), 8076–8083. <https://doi.org/10.1021/jp100013h>.
- (80) Bannwarth, C.; Ehlert, S.; Grimme, S. GFN2-XTB - An Accurate and Broadly Parametrized Self-Consistent Tight-Binding Quantum Chemical Method with Multipole Electrostatics and Density-Dependent Dispersion Contributions. *J. Chem. Theory Comput.* **2019**, *15* (3), 1652–1671. <https://doi.org/10.1021/acs.jctc.8b01176>.
- (81) Parimalam, B. S.; MacIntosh, A. D.; Kadam, R.; Lucht, B. L. Decomposition Reactions of Anode Solid Electrolyte Interphase (SEI) Components with LiPF₆. *J. Phys. Chem. C* **2017**, *121* (41), 22733–22738. <https://doi.org/10.1021/acs.jpcc.7b08433>.
- (82) Zhuang, G. V.; Yang, H.; Ross, P. N.; Xu, K.; Jow, T. R. Lithium Methyl Carbonate as a Reaction Product of Metallic Lithium and Dimethyl Carbonate. *Electrochem. Solid-State Lett.* **2006**, *9* (2). <https://doi.org/10.1149/1.2142157>.
- (83) Banerjee, A.; Wang, X.; Fang, C.; Wu, E. A.; Meng, Y. S. Interfaces and Interphases in All-Solid-State Batteries with Inorganic Solid Electrolytes. *Chem. Rev.* **2020**, *120* (14), 6878–6933. <https://doi.org/10.1021/acs.chemrev.0c00101>.
- (84) Yim, T.; Woo, S. G.; Lim, S. H.; Cho, W.; Song, J. H.; Han, Y. K.; Kim, Y. J. 5V-Class High-Voltage Batteries with over-Lithiated Oxide and a Multi-Functional Additive. *J. Mater. Chem. A* **2015**, *3* (11), 6157–6167. <https://doi.org/10.1039/c4ta06531j>.
- (85) Park, M. W.; Park, S.; Choi, N. S. Unanticipated Mechanism of the Trimethylsilyl Motif in Electrolyte Additives on Nickel-Rich Cathodes in Lithium-Ion Batteries. *ACS Appl. Mater. Interfaces* **2020**, *12* (39), 43694–43704. <https://doi.org/10.1021/acsami.0c11996>.
- (86) Han, Y. K.; Yoo, J.; Yim, T. Why Is Tris(Trimethylsilyl) Phosphite Effective as an Additive for High-Voltage Lithium-Ion Batteries? *J. Mater. Chem. A* **2015**, *3* (20), 10900–10909. <https://doi.org/10.1039/c5ta01253h>.
- (87) Qi, X.; Tao, L.; Hahn, H.; Schultz, C.; Gallus, D. R.; Cao, X.; Nowak, S.; Röser, S.; Li, J.; Cekic-Laskovic, I.; Rad, B. R.; Winter, M. Lifetime Limit of Tris(Trimethylsilyl) Phosphite as Electrolyte Additive for High Voltage Lithium Ion Batteries. *RSC Adv.* **2016**, *6* (44), 38342–38349. <https://doi.org/10.1039/c6ra06555d>.

Acta Universitatis Upsaliensis

Digital Comprehensive Summaries of Uppsala Dissertations from the Faculty of Science and Technology 2365

Editor: The Dean of the Faculty of Science and Technology

A doctoral dissertation from the Faculty of Science and Technology, Uppsala University, is usually a summary of a number of papers. A few copies of the complete dissertation are kept at major Swedish research libraries, while the summary alone is distributed internationally through the series Digital Comprehensive Summaries of Uppsala Dissertations from the Faculty of Science and Technology. (Prior to January, 2005, the series was published under the title "Comprehensive Summaries of Uppsala Dissertations from the Faculty of Science and Technology".)



Distribution: publications.uu.se
urn:nbn:se:uu:diva-523121

ACTA UNIVERSITATIS
UPSALIENSIS
2024